

Carderock Division
Naval Surface Warfare Center

Bethesda, Maryland 20084-5000

NSWCCD-SIG-96/061-7030 May 1996
Signatures Directorate
Research and Development Report

**Use of the Double-Sum Technique for
Computing the Modal Response of Regularly
Ribbed Cylinders**

by

G. Maidanik
K.J. Becker

DTIC QUALITY INSPECTED 2

19961015 020



Approved for public release; Distribution is unlimited.

UNCLASSIFIED

SECURITY CLASSIFICATION OF THIS PAGE

REPORT DOCUMENTATION PAGE

Form Approved
OMB No. 0704-0188

1a. REPORT SECURITY CLASSIFICATION Unclassified		1b. RESTRICTIVE MARKINGS None	
2a. SECURITY CLASSIFICATION AUTHORITY		3. DISTRIBUTION / AVAILABILITY OF REPORT Approved for public release.	
2b. DECLASSIFICATION/DOWNGRADING SCHEDULE		Distribution is unlimited.	
4. PERFORMING ORGANIZATION REPORT NUMBER(S) NSWCCD-SIG-96/061-7030		5. MONITORING ORGANIZATION REPORT NUMBER(S)	
6a. NAME OF PERFORMING ORGANIZATION NSWC, Carderock Division	6b. OFFICE SYMBOL (If applicable) Code 7030	7a. NAME OF MONITORING ORGANIZATION	
c. ADDRESS (City, State, and ZIP Code) Bethesda, MD 20084-5000		7b. ADDRESS (City, State, and ZIP Code)	
8a. NAME OF FUNDING/SPONSORING ORGANIZATION	8b. OFFICE SYMBOL (If applicable)	9. PROCUREMENT INSTRUMENT IDENTIFICATION NUMBER	
c. ADDRESS (City, State, and ZIP Code)		10. SOURCE OF FUNDING NUMBERS	
		PROGRAM ELEMENT NO.	PROJECT NO.
		TASK NO.	WORK UNIT ACCESSION NO.
1. TITLE (Include Security Classification) Use of the Double-Sum Technique for Computing the Modal Response of Regularly Ribbed Cylinders			
2. PERSONAL AUTHOR(S) G. Maidanik and K.J. Becker			
13a. TYPE OF REPORT Research & Development	13b. TIME COVERED FROM 960101 TO 960531	14. DATE OF REPORT (Year, Month, Day) 1996 May 31	15. PAGE COUNT 55
16. SUPPLEMENTARY NOTATION			
17. COSATI CODES		18. SUBJECT TERMS (Continue on reverse if necessary and identify by block number) Structural Acoustics Fourier Transform Double-Sum Wave Propagations	
19. ABSTRACT (Continue on reverse if necessary and identify by block number) Recently an efficient technique was proposed for performing a Fourier transformation on integrands that are composed of aliased factors. In this report the proposed technique is utilized to perform Fourier transformations on quantities that pertain to the response of a regularly ribbed cylinder. The computations relate to Fourier transformations from the axial wavenumber domain to the axial spatial domain. The phenomena of aliasing and pass and stop bands are of particular interest. It is argued that the complementarity of the data, when presented in the two Fourier conjugate domains, may be a useful analytical (and experimental) tool.			
20. DISTRIBUTION / AVAILABILITY OF ABSTRACT <input checked="" type="checkbox"/> UNCLASSIFIED/UNLIMITED <input type="checkbox"/> SAME AS RPT. <input type="checkbox"/> DTIC USERS		21. ABSTRACT SECURITY CLASSIFICATION Unclassified	
22a. NAME OF RESPONSIBLE INDIVIDUAL Maidanik, G.		22b. TELEPHONE (Include Area Code) (301) 227-1292	22c. OFFICE SYMBOL NSWCCD 7030

CONTENTS

	Page
ABSTRACT.....	1
I. INTRODUCTION	2
II. MODAL RESPONSE OF A RIBBED CYLINDER.....	9
III. MODAL RESPONSE OF A UNIFORM CYLINDER IN THE SPATIAL DOMAIN	21
IV. MODAL DRIVE IN LIEU OF THE RIBS IN THE SPATIAL DOMAIN	25
V. RESPONSE OF A REGULARLY RIBBED CYLINDER IN THE SPATIAL DOMAIN	28
REFERENCES	49

ABSTRACT

Recently an efficient technique was proposed for performing a Fourier transformation on integrands that are composed of aliased factors. In this report the proposed technique is utilized to perform Fourier transformations on quantities that pertain to the response of a regularly ribbed cylinder. The computations relate to Fourier transformations from the axial wavenumber domain to the axial spatial domain. The phenomena of aliasing and pass and stop bands are of particular interest. It is argued that the complementarity of the data, when presented in the two Fourier conjugate domains, may be a useful analytical (and experimental) tool.

I. INTRODUCTION

In a recent report the authors proposed a novel computational technique to perform a certain class of Fourier transformations [1]. The class pertains to Fourier transformations in which the integrands are completely or partially composed of terms and factors that are aliased with respect to a specific scale factor in the domain in which the integrand is expressed. This class harbors a number of phenomena in structural acoustics. A few of these phenomena are employed in this report to exemplify the use of the double-sum technique for computing Fourier transforms [1]. In particular, the circumferential modal response of a regularly ribbed cylinder is transformed from the k -domain into the x -domain. These Fourier conjugate domains lie in the axial direction of the cylinder. The phenomena of special concern in the present report are those relating to aliasing and pass and stop bands in that modal response [2-6]. Hybrid and natural cylinders are exemplified. A hybrid cylinder is defined by analytically removing the membrane free waves from the cylinder. In this sense, the mechanical response of a hybrid cylinder is akin to that of a panel that is enjoying the same plating [2]. This report assumes that the descriptions of these phenomena and the analytical models of the cylindrical structures are familiar to the reader; nonetheless a cursory analytical development is included. A more detailed analytical development can be found in References 2-6. However, the analytical development of the double-sum technique that is presented in Reference 1 is not repeated here; Reference 1 is considered an essential companion to this report and the reference to equations in Reference 1 are prefaced by unity. Thus, Eq. (6) in Reference 1 is designated Eq. (1-6) in the present report. The physical construction of the externally driven ribbed cylinder and the chosen coordinate system are sketched and depicted in Fig. 1, respectively.

In Section II the response and the external drive that generate it are expanded in terms of circumferential eigenfunctions [7]. The coefficients in these expansions are the modal responses and modal external drives. The modal properties of the cylindrical shell

that relate the modal response to the corresponding modal external drive are defined; this relationship defines the modal impulse response function. It is argued that for a regularly ribbed cylinder, the expressions for the impulse response function and its terms and factors are readily stated and interpreted in the $\{k, n, \omega\}$ -domain, where (ω) is the frequency variable, (n) is the mode index and (k) is the axial wavenumber variable [8]. Indeed, in this domain the relationship between the modal response $V_n(k, \omega)$ and the modal external drive $P_{en}(k, \omega)$ may be expressed in the form

$$V_n(k, \omega) = G_{\infty n}(k, \omega) [P_{en}(k, \omega) - P_{sn}(k, \omega)] ,$$

where $P_{sn}(k, \omega)$ is the drive in lieu of the ribs and $G_{\infty n}(k, \omega)$ is the modal admittance of the uniform (unribbed) cylinder. The external drive is adequately defined in the simple form

$$P_{en}(k, \omega) = P_{en}^o(\omega) \exp(ikx_a) ,$$

where (x_a) is the position, in the x -domain, to which the external drive is applied and it is assumed that the modal strength $P_{en}^o(\omega)$ is independent of (k) . The uniform cylinder modal admittance $G_{\infty n}(k, \omega)$ comprises two distinct terms; the modal mechanical surface impedance $Z_{pn}(k, \omega)$ and the modal fluid surface impedance $Z_n^f(k, \omega)$ on the outside surface of the cylinder

$$G_{\infty n}(k, \omega) = [Z_{pn}(k, \omega) + Z_n^f(k, \omega)]^{-1} .$$

On the inside of the cylinder vacuum is assumed to prevail. The modal mechanical surface impedance $Z_{pn}(k, \omega)$, in turn, also comprises two terms

$$Z_{pn}(k, \omega) = Z_n^p(k, \omega) + Z_n^m(k, \omega) ,$$

where $Z_n^p(k, \omega)$ is the modal flexural surface impedance and $Z_n^m(k, \omega)$ is the membrane surface impedance [8-10]. When the membrane surface impedance is analytically removed; $Z_n^m(k, \omega) = 0$, the admittance $G_{\infty n}(k, \omega)$, given now by

$$G_{\infty n}(k, \omega) = [Z_n^p(k, \omega) + Z_n^f(k, \omega)]^{-1} ,$$

describes the fluid loaded modal admittance of a uniform (unribbed) hybrid cylinder.

The drive $P_{sn}(k, \omega)$ in lieu of the ribs is not only a functional of the properties of the uniform cylinder; defined by $G_{\infty n}(k, \omega)$, but is naturally also a functional of the properties of the ribs. In a regularly ribbed cylinder the properties of the ribs are defined in terms of the modal line impedance $Z_{sn}(\omega)$ and the separation distance (b) between adjacent ribs. This line impedance can be either mass, resistance or stiffness controlled; the change from one characteristic to another is frequency dependent [11]. The modal drive $P_{sn}(k, \omega)$, in addition, is a functional of the external drive. In the definition of the external drive here proposed, the dependence on the position of application (x_a) is of particular significance.

It is convenient to normalize the modal response in the form

$$\bar{V}_n(k, \omega) = \bar{V}_{\infty n}(k, \omega) - \bar{V}_{sn}(k, \omega) = \bar{G}_{sn}(k, \omega) [\bar{P}_{en}(k, \omega) - \bar{P}_{sn}(k, \omega)] ;$$

$$\bar{V}_{\infty n}(k, \omega) = \bar{G}_{\infty n}(k, \omega) \bar{P}_{en}(k, \omega) ; \quad \bar{V}_{sn}(k, \omega) = \bar{G}_{\infty n}(k, \omega) \bar{P}_{sn}(k, \omega) .$$

This normalization of the modal response is achieved by the appropriate normalization of its constituent terms and factors, namely

$$\bar{V}_n(k, \omega) = [V_n(k, \omega) / V_{on}(\omega)] ; \quad V_{on}(\omega) = [P_{en}^o(\omega) / (i\omega m)] ;$$

$$\bar{G}_{\infty n}(k, \omega) = [(i\omega m) G_{\infty n}(k, \omega)] ; \quad \bar{P}_{sn}(k, \omega) = [P_{sn}(k, \omega) / P_{en}^o(\omega)] ,$$

where $(i\omega m)$ is the surface mass impedance of the plating of the cylinder and $P_{en}^o(\omega)$, as already mentioned, is the strength of the modal external drive.

The absolute values of $\bar{V}_{\infty n}(k, \omega)$, or equivalently $\bar{G}_{\infty n}(k, \omega)$, of $\bar{P}_{sn}(k, \omega)$ and of $\bar{V}_n(k, \omega)$ are computed and displayed as functions of (ak) in a frequency waterfall format, where (a) is the radius of the cylinder [12]. The frequency (ω) is normalized by the critical frequency (ω_c) of the flexural free waves with respect to the speed of sound (c) in the fluid. The discussions of these and other presentations in this report are limited to the frequency range defined by

$$(2\omega_r / \omega_c) \leq (\omega / \omega_c) \leq 0.6 ; \quad \omega_r = (c_t / a) ,$$

and to the wavenumber range defined by

$$0 \leq (ak) \leq 75 ,$$

where ω_r is the ring frequency of the cylinder. The speed $c_t = \{Yh/m\}/(1-v^2)\}^{1/2}$, where Y , v , m and h are the Young's modulus, the Poisson's ratio, the surface mass and the thickness of the plating of the cylinder, respectively, is the longitudinal speed in that plating. One may find it convenient to list a set of standard parametric values to define standard displays. When variations in the parametric values are instituted, it is necessary

to report only those parameters that are varied. The remaining parameters are assumed to maintain standard values.

The normalized modal response $\bar{V}_{\infty n}(k, \omega)$ of a uniform (unribbed) cylinder under standard parametric values, and a few specific variations on these parametric values, are presented in Figs. 2 and 3. The first set; i.e., Fig. 2, pertains to a hybrid cylinder and the second set; i.e., Fig. 3, pertains to a natural cylinder. The footprints of fluid loading and membrane free waves are of particular interest in these two sets of figures.

The normalized modal drive $\bar{P}_{sn}(k, \omega)$ in lieu of the ribs under standard parametric values, and a few specific variations on these parametric values, are presented in Figs. 4 and 5. The third set; i.e., Fig. 4, pertains to a hybrid cylinder and the fourth set; i.e., Fig. 5, pertains to a natural cylinder. The footprints of aliasing and stop and pass bands are of particular interest in these two figures.

The normalized modal response $\bar{V}_n(k, \omega)$ of the regularly ribbed cylinder under standard parametric values, and a few specific variations on these parametric values, are presented in Figs. 6 and 7. The fifth set; i.e., Fig. 6, pertains to a hybrid cylinder and the sixth set; i.e., Fig. 7, pertains to a natural cylinder. The footprints of the normalized drive $\bar{P}_{sn}(k, \omega)$, as depicted in Figs. 4 and 5, are clearly discernible in the normalized response $\bar{V}_n(k, \omega)$. However, the strict aliasing in the drive is impaired in the response. This defect is perpetrated by the term that describes the normalized modal response $\bar{V}_{\infty n}(k, \omega)$ in the absence of ribs and by the factor $\bar{G}_{\infty n}(k, \omega)$ that multiplies the normalized aliased modal drive $\bar{P}_{sn}(k, \omega)$; neither the term nor the factor are aliased quantities. Does the impairment of the aliasing in $\bar{V}_n(k, \omega)$ imply a corresponding defect in the pass and stop bands of the modal response as compared with that exhibited by the modal drive in lieu of the ribs? The answer to this question is sought, in part, by using complementarity to Figs. 2 through 7. This complementarity is derived by a Fourier transformation of $\bar{V}_{\infty n}(k, \omega) = [\bar{G}_{\infty n}(k, \omega) \bar{P}_{en}(k, \omega)]$, $\bar{P}_{sn}(k, \omega)$ and $\bar{V}_n(k, \omega)$ into $\bar{v}_{\infty n}(x, \omega)$, $\bar{p}_{sn}(x, \omega)$ and $\bar{v}_n(x, \omega)$, respectively. The Fourier transformation of

these quantities is carried out in terms of the double-sum technique developed in Reference 1.

In Section III the procedure for computing $\bar{v}_{\infty n}(x, \omega)$, by a Fourier transformation of $\bar{V}_{\infty n}(k, \omega)$, is explained and the results are displayed in Figs. 8 through 10. Several variations in the parametric values are investigated and comparisons between Figs. 2 and 3 that feature $\bar{V}_{\infty n}(k, \omega)$ and the corresponding Figs. 8 through 10 that feature $\bar{v}_{\infty n}(x, \omega)$ are conducted and discussed. Interferences between flexural, fluid and membrane free waves at regions where their amplitudes are of comparable strengths are of particular interest. Such interferences are revealed when the dominant flexural free waves are subdued by selectively increasing the damping that is assigned to them. It is thus found that a complemental investigation of $\bar{V}_{\infty n}(k, \omega)$ and $\bar{v}_{\infty n}(x, \omega)$ is an analytical tool of value.

In Section IV the procedure for computing $\bar{p}_{sn}(x, \omega)$ by a Fourier transformation of $\bar{P}_{sn}(k, \omega)$, is explained and the results are displayed in Figs. 4, 5, 11 and 12. In Figs. 4 and 5 computations of $\bar{p}_{sn}(x, \omega)$ are superimposed, frequency-wise, on the corresponding figures that display $\bar{P}_{sn}(k, \omega)$. Figures 4 and 5 exhibit clearly the phenomena of aliasing and pass and stop bands. The complementarity between the Fourier conjugate pairs, $\bar{P}_{sn}(k, \omega)$, on the one hand, and $\bar{p}_{sn}(x, \omega)$, on the other, are more directly and simultaneously contrasted in these figures. The value of complementarity as an analytical tool is thus supported in Figs. 4 and 5. The influence of fluid loading on the phenomenon of pass and stop bands is investigated in Figs. 11 and 12. Moreover, the bottoming of the flexural stop bands by the fluid and membrane free waves are discernible in these figures.

In Section V the procedure for computing $\bar{v}_n(x, \omega)$ by a Fourier transformation of $\bar{V}_n(k, \omega)$, is explained and the results are displayed in Figs. 13 through 15. Of particular interest is the bottoming of the response in a flexural stop band by the fluid and membrane free waves. The similarity of this bottoming to the corresponding bottoming

induced by damping the flexural free waves, is striking. [cf. Figs. 8 through 10 and 13 through 15.] The complementarity between Figs. 6 and 7 and the corresponding Figs. 13 through 15, again shows the value of its employment. Of particular interest in this final section are the comparisons between Figs. 4 and 5 and 11 and 12, on the one hand, and Figs. 6 and 7 and 13 through 15, on the other. These comparisons reveal that the impairment of the aliasing patterns in $\bar{V}_n(k, \omega)$, as compared with those in $\bar{P}_{sn}(k, \omega)$, is not duplicated in the pass and stop bands in $\bar{v}_n(x, \omega)$, as compared with those in $\bar{p}_{sn}(x, \omega)$. Indeed, if at all, the phenomenon of pass and stop bands in $\bar{v}_n(x, \omega)$ is sharper than it is in $\bar{p}_{sn}(x, \omega)$.

II. MODAL RESPONSE OF A RIBBED CYLINDER

The circumferential uniformity and finiteness of the cylinder, unribbed and ribbed, allow quantities to be expanded in terms of circumferential eigenfunctions $\Phi_n(\phi)$, where ϕ is the circumferential variable as shown in Fig. 1. Thus, the response $v(x, \phi, \omega)$ and the external drive $p_e(x, \phi, \omega)$ can be modalized in the x -domain

$$v(x, \phi, \omega) = \sum_n \Phi_n(\phi) v_n(x, \omega) ;$$

$$p_e(x, \phi, \omega) = \sum_n \Phi_n(\phi) p_{en}(x, \omega) , \quad (1a)$$

and in the k -domain

$$V(k, \phi, \omega) = \sum_n \Phi_n(\phi) V_n(k, \omega) ;$$

$$P_e(k, \phi, \omega) = \sum_n \Phi_n(\phi) P_{en}(k, \omega) . \quad (1b)$$

Quantities in Eq. (1) are related Fourier transforms; in particular

$$v_n(x, \omega) = (2\pi)^{-1/2} \int dk \exp(-ixk) V_n(k, \omega) , \quad (2a)$$

$$p_{en}(x, \omega) = (2\pi)^{-1/2} \int dk \exp(-ixk) P_{en}(k, \omega) . \quad (2b)$$

The circumferential eigenfunctions $\Phi_n(\phi)$, are assumed to be orthogonal and complete

$$\int \Phi_n(\phi) d\phi \Phi_m^*(\phi) = \delta_{nm} ; \quad \sum_n \Phi_n(\phi) \Phi_n^*(\phi') = \delta(\phi - \phi') ;$$

$$0 \leq (\phi - \phi') < 2\pi , \quad (3)$$

where δ_{nm} and δ are the Kronecker delta and the delta function, respectively [8]. The modal response $v_n(x, \omega)$ of the cylinder to the modal external drive $p_{en}(x, \omega)$ in the x -domain can be formally expressed in the form

$$v_n(x, \omega) = \int g_n(x | x', \omega) dx' p_{en}(x', \omega) , \quad (4a)$$

and in the k -domain in the form

$$V_n(k, \omega) = \int G_n(k | k', \omega) dk' P_{en}(k', \omega) , \quad (4b)$$

where, in addition to Eq.(2), the impulse response functions in these equations are related Fourier transforms; e.g.,

$$g_n(x | x', \omega) = (2\pi)^{-1} \int dk \int dk' \exp[-i(xk - x'k')] G_n(k | k', \omega) . \quad (5)$$

It is convenient to normalize the modal impulse response function by the surface mass impedance ($i\omega m$) of the plating of the cylinder and the modal drive by the modal ring drive $P_{en}^o(\omega)$; namely

$$\bar{G}_n(k \mid k', \omega) = (i\omega m) G_n(k \mid k', \omega) ;$$

$$\bar{P}_{en}(k, \omega) = [P_{en}(k, \omega) / P_{en}^o(\omega)] = \exp(ix_a k) , \quad (6a)$$

where (m) is the surface mass of the plating and (x_a) is the position of the ring to which the modal external drive is applied. The normalization of the modal response $V_n(k, \omega)$ follows

$$\bar{V}_n(k, \omega) = [V_n(k, \omega) / V_{no}(\omega)] ; \quad V_{no}(\omega) = [P_{en}^o(\omega) / (i\omega m)] . \quad (6b)$$

The modal impulse response function $\bar{G}_n(k \mid k', \omega)$ for a regularly ribbed cylinder is readily derived in the k -domain in the simple operator form

$$\bar{G}_n(k \mid k', \omega) = \bar{G}_{\infty n}(k, \omega) [1 - S_b(k) \{I_{bn}(k, \omega) Q_{\infty n}(k, \omega)\}] \delta(k - k') , \quad (7)$$

where

$$Q_{\infty n}(k, \omega) = [Z_{sn}(\omega) / b] G_{\infty n}(k, \omega) , \quad (8a)$$

$$I_{bn}(k, \omega) = [1 + S_b(k) \{Q_{\infty n}(k, \omega)\}]^{-1} , \quad (8b)$$

the wavenumber operator $S_b(k)$ is defined in Eq.(1-3), (b) is the separation distance between adjacent ribs, $Z_{sn}(\omega)$ is the modal ring impedance of the ribs, and $\bar{G}_{\infty n}(k, \omega)$ is

the normalized modal surface admittance of the uniform (unribbed) cylinder. The incomplete curly brackets preceded by the wavenumber operator $S_b(k)$ in Eq. (7) merely indicates that the wavenumber operation to be performed is yet to be completed; indeed, $\bar{G}_n(k \mid k', \omega)$ is a wavenumber operator and not just an algebraic factor. The normalized quantity $\bar{G}_{\infty n}(k, \omega)$ is the inverse of three terms

$$\begin{aligned} \bar{G}_{\infty n}(k, \omega) &= (i\omega m) G_{\infty n}(k, \omega) = \\ &[\bar{Z}_n^p(k, \omega) + \bar{Z}_n^m(k, \omega) + \bar{Z}_n^f(k, \omega)]^{-1}, \end{aligned} \quad (9a)$$

where $\bar{Z}_n^p(k, \omega)$, $\bar{Z}_n^m(k, \omega)$ and $\bar{Z}_n^f(k, \omega)$ are the normalized flexural, membrane and fluid modal surface impedances, respectively, of the uniform cylinder. A hybrid cylinder is defined by a (natural) cylinder from which the membrane free waves are analytically removed by setting $\bar{Z}_n^m(k, \omega)$ equal to zero in Eq. (9a). A hybrid cylinder is defined by a normalized modal surface admittance

$$\bar{G}_{\infty n}(k, \omega) = [\bar{Z}_n^p(k, \omega) + \bar{Z}_n^f(k, \omega)]^{-1}; \quad \bar{Z}_n^m(k, \omega) = 0. \quad (9b)$$

Recognizing that the mechanical surface impedance $\bar{Z}_p(k, k_y, \omega)$ for a uniform panel relates to $\bar{Z}_n^p(k, \omega)$ in the form

$$\bar{Z}_p(k, (n/a), \omega) \equiv \bar{Z}_n^p(k, \omega), \quad (10)$$

and that the fluid surface impedance $\bar{Z}_f(k, (n/a), \omega)$ on a panel qualitatively relates to $\bar{Z}_n^f(k, \omega)$, it is inferred that a hybrid cylinder is akin to a panel, and in some cases, the results obtained on a hybrid cylinder can be inferentially translated to those on a panel [2]. The quantity $Q_{\infty n}(k, \omega)$ is the ratio of the equivalent modal surface impedance

$[Z_{sn}(\omega)/b]$ of a rib to the modal surface impedance $[G_{\infty n}(k, \omega)]^{-1}$ of the uniform cylinder. It is convenient to express $Z_{sn}(\omega)$ in the form

$$Z_{sn}(\omega) = (i\omega M) A_n(\omega/\omega_n) , \quad (11)$$

and hence from Eq. (8a) one derives

$$Q_{sn}(k, \omega) = (M/m b) A_n(\omega/\omega_n) , \quad (8c)$$

where M is a line mass and $A_n(\omega/\omega_n)$ is a resonance bearing factor. In this report $A_n(\omega/\omega_n)$ is equivalently set either to unity or to $-[1 + (\alpha_n \omega/\omega_n)^2]^{-1}$, the ring impedance of the ribs in the former setting is mass controlled and in the latter stiffness controlled [2]. Substituting Eq. (7) in Eq. (4b) one derives

$$\bar{V}_n(k, \omega) = \bar{V}_{\infty n}(k, \omega) - \bar{V}_{sn}(k, \omega) , \quad (12)$$

$$\bar{V}_{\infty n}(k, \omega) = \bar{G}_{\infty n}(k, \omega) \exp(ix_a k) , \quad (13a)$$

$$\bar{V}_{sn}(k, \omega) = \bar{G}_{\infty n}(k, \omega) \bar{P}_{sn}(k, \omega) , \quad (13b)$$

where

$$\begin{aligned} \bar{P}_{sn}(k, \omega) &= [P_{sn}(k, \omega) / P_{en}^o(\omega)] = \\ &S_b(k) \{I_{bn}(k, \omega) Q_{\infty n}(k, \omega) \exp(ix_a k)\} , \end{aligned} \quad (14a)$$

is the normalized modal drive in lieu of the ribs. Clearly, $\bar{P}_{sn}(k, \omega)$ is an aliased quantity in (k) with respect to (κ_1) ; $\kappa_1 = (2\pi/b)$. [cf. Eq. (1-17a).] Moreover, one recognizes

that $I_{bn}(k, \omega)$ as stated in Eq. (8b) is similarly aliased in (k) with respect (κ_1) . [cf. Eq. (1-19a).] In consequence $\bar{P}_{sn}(k, \omega)$ can be factorized in the form

$$\bar{P}_{sn}(k, \omega) = I_{bn}(k, \omega) S_b(k) \{Q_{\infty n}(k, \omega) \exp(ix_a k)\} . \quad (14b)$$

[cf. Eq. (1-18a).] It is apparent from Eqs. (12) through (14) that the behavior of the modal response $\bar{V}_n(k, \omega)$ and a number of terms and factors in its composition; e.g., the modal response $\bar{V}_{\infty n}(k, \omega)$ in the absence of ribs and the drive $\bar{P}_{sn}(k, \omega)$ in lieu of the ribs, are merely functional of the properties of the fluid loaded uniform cylinder, the ribs and the external drive. These properties are described by the modal surface admittance $G_{\infty n}(k, \omega)$ of the uniform cylinder, the modal line impedance $Z_{sn}(\omega)$ and the separation distance (b) of the ribs and the ring position (x_a) of the external drive. The absolute values of the quantities $\bar{V}_{\infty n}(k, \omega)$ or equivalently $\bar{G}_{\infty n}(k, \omega)$, $\bar{P}_{sn}(k, \omega)$ and $\bar{V}_n(k, \omega)$, as functions of (ak) , are computed and presented in typical frequency waterfall displays in Figs. 2 and 3, 4 and 5, and 6 and 7, respectively [12]. The even numbered figures in each set; e.g., Fig. 2, relate to a hybrid cylinder and the odd numbered; e.g., Fig. 3, relate to a natural cylinder. A typical case is defined by standard parametric values. These standard values may also serve to define other cases by merely selecting changes in specific standard values. The standard parametric values and their definitions follow: the flexural free waves are defined by a wavenumber k_p ,

$$k_p = k_{po}(1-i\eta_p) ; \quad k_{po}^2 = (\omega\omega_c / c^2) ;$$

$$(h/a) = 10^{-2} ; \quad \eta_p = 10^{-3} , \quad (15a)$$

the longitudinal free waves are defined by a wavenumber k_ℓ ,

$$k_\ell = k_{\ell o}(1 - i\eta_\ell) ; \quad k_{\ell o} = (\omega / c_\ell) ; \quad c_\ell^2 = (Y / \rho_s)(1 - \nu^2)^{-1} ;$$

$$m = h\rho_s ; \quad (c_\ell / c) = 3.5 ; \quad \eta_\ell = 5 \times 10^{-4} , \quad (15b)$$

the shear free waves are defined by a wavenumber k_s ,

$$k_s = k_{so}(1 - i\eta_s) ; \quad k_{so} = (\omega / c_s) ; \quad (c_s / c_\ell)^2 = [(1 - \nu) / 2] ;$$

$$\nu = (1/3) ; \quad \eta_s = 5 \times 10^{-4} , \quad (15c)$$

the fluid loading is defined by a fluid loading parameter ε_c ,

$$\varepsilon_c = (\rho c / \omega_c m) ; \quad (a\omega_c / c) = 97.53 ; \quad \varepsilon_c = 10^{-2} , \quad (15d)$$

the ring frequency ω_r and the critical frequency ω_c are defined

$$\omega_r = (c_\ell / a) ; \quad \omega_c = \sqrt{12} (c^2 / hc_\ell) ;$$

$$(\omega_r / \omega_c) = 3.6 \times 10^{-2} , \quad (15e)$$

and the definition of the ribs and mode index (n) are specified

$$(b / a) = 0.3 ; \quad (M / mb) = 0.2 ; \quad (x_a / b) = 0.5 ;$$

$$A_n(\omega / \omega_n) = 1 ; \quad n = 1 , \quad (15f)$$

where (a) is the radius, Y is Young's modulus, (v) is the Poisson's ratio and (ρ_s) is the density of the plating of the cylinder and (ρ) and (c) are the density and sound speed in the fluid. The interest in this report is confined to the spectral range

$$\{0, (2\omega_r / \omega_c)\} \leq \{(ak), (\omega / \omega_c)\} \leq \{75, 0.6\}, \quad (15g)$$

notwithstanding that some displays are extended, but not discussed, into the frequency range $(\omega / \omega_c) \leq (2\omega_r / \omega_c)$. Computations and their representations in this low frequency are discussed under a separate cover [2]. The first sub-figures in the first and second sets; i.e., Figs. 2a and 3a, are computed under standard parametric values. The flexural free waves and the fluid free waves are clearly discernible in Fig. 2a. In Fig. 3a, in addition to the flexural and fluid free waves, membrane free waves are clearly discernible. The membrane free waves comprise the longitudinal and shear free waves. "Curvature free waves" that supersede the flexural free waves and the origins and the higher surface impedances of the membrane free waves are found largely to reside, in Fig. 3a, in the low frequency range; $(\omega / \omega_c) \leq (2\omega_r / \omega_c)$. Again, discussion of these features are not conducted in this report [2]. Figures 2a and 3a are repeated in Figs. 2b and c and 3b and c, respectively, except that the fluid loading parameter (ε_c) is changed from the standard value of 10^{-2} to 10^{-4} and 10^{-1} , respectively. In this connection it is observed that a fluid loading with $\varepsilon_c = 10^{-4}$ is light, with $\varepsilon_c = 10^{-2}$ is moderate and with $\varepsilon_c = 10^{-1}$ is heavy. The change of (ε_c) from 10^{-2} to 10^{-4} renders the fluid free waves hardly discernible in Figs. 2b and 3b, little else is different between these figures and Figs. 2a and 3a, respectively. The change of (ε_c) from 10^{-2} to 10^{-1} intensifies the fluid free waves in Figs. 2c and 3c. Moreover, this change in fluid loading shifts the free waves, especially the subsonic flexural waves, to a higher wavenumber range and weakens the strengths of the supersonic membrane free waves. The shifts are due to the "added surface mass" and the weakening is due to the "radiation damping" effects

associated with the fluid loading. Figures 2d and 3d repeat Figs. 2a and 3a, respectively, except that the flexural loss factor (η_p) is changed from the standard value of 10^{-3} to 3×10^{-2} ; a substantial increase in the damping of the flexural free waves. Indeed, the flexural free waves in Figs. 2d and 3d are substantially subdued compared with those in Figs. 2a and 3a. Figures 2a and 3a are repeated in Figs. 2e and 3e, respectively, except that the mode index (n) is changed from the standard value of unity to zero. This change hardly induces any change in the flexural free waves; however, a drastic change is induced in the membrane free waves. The membrane free waves in Fig. 3a are comprised of longitudinal and shear free waves, in Fig. 3e of longitudinal free waves only. The shear free waves join the longitudinal when the mode index (n) equals to or exceeds unity. Thus, in Fig. 3f, which repeats Fig. 3a except that the mode index (n) is set equal to (2), the membrane free waves are composed of both, the longitudinal and shear free waves. Finally, the first set is completed by Fig. 3g. This figure repeats Fig. 3e, except that the flexural loss factor (η_p) is changed from the standard value of 10^{-3} to 3×10^{-2} . Again, the flexural free waves are substantially subdued by this change. [cf. Figs. 2d and 3d.]

The first sub-figures in the third and fourth sets; i.e., Figs. 4a and 5a, are computed under standard parametric values. The aliasing of the normalized modal drive $\bar{P}_{sn}(k, \omega)$ in lieu of the ribs is apparent in these figures; the dominant patterns are those associated with the flexural free waves. Nonetheless, aliasing in the membrane free waves are discernible in Fig. 5a. Aliasing is basically a scattering phenomenon and although the aliasing patterns of the membrane free waves are scant, the scattering of the membrane free waves by “simple” ribs are clearly established in Fig. 5a. In part, the visibility of the membrane free waves in Fig. 5a is aided by the locus minima in $\bar{P}_{sn}(k, \omega)$. These locus minima occur in $\bar{P}_{sn}(k, \omega)$, in both Figs. 4a and 5a, whenever $(ak) = \pm (a\kappa_1) [(2j+1)/2]$ and is due to the symmetry in this quantity. The symmetry results from the standard position of the external drive at $(x_a/b) = 0.5$.

This symmetry is removed in Figs. 4b and 5b. These figures repeat Figs. 4a and 5a, respectively, except that (x_a/b) is changed from 0.5 to 0.3. The locus of minima are absent in the patterns of Figs. 4b and 5b. Moreover, the patterns relating to the membrane free waves in Fig. 5b are weakened. The fluid free waves are hardly discernible in Figs. 4a and b and 5a and b. A major feature in the patterns of these figures is the cancellations between the peaks of a pair of flexural aliasing orders in the region in which they cross. Regions of these kind lie regularly in certain frequency bands. The cancellations are made possible by the interactions of the ribs among themselves via the cylindrical shells; in the absence of such interactions the cancellations are also absent [2,13]. Figures 4a and 5a are repeated in Figs. 4c and 5c respectively, except that the fluid loading parameter is increased from the standard value of 10^{-2} to 10^{-1} . The influence of this increase is largely discernible in the shifts in the frequency bands at which pairs of various flexural aliasing orders cross; the shifts are to lower frequencies and are consistent with the wavenumber shifts observed between Figs. 2a and 3a and Figs. 2c and 3c. In addition, the flexural free waves in both figures and the membrane free waves in Fig. 5c are subdued by this increase in the fluid loading. Remembering that under the influence of ribs the subsonic flexural free waves can become reasonable radiators, the subdued flexural and, again, the membrane free waves can be attributed to the increase in radiation damping with the increase in fluid loading. However, the fluid free waves, as such, are still hardly discernible in Figs. 4c and 5c. [cf. Figs. 4a and b and 5a and b, respectively.] Figures 4d and 5d repeat Figs. 4a and 5a, except that the standard mass controlled ring impedance of the ribs; i.e., with $A_n(\omega/\omega_n) = 1$, is changed to that of stiffness controlled; i.e., with $A_n(\omega/\omega_n) = -[1+(5\omega/\omega_c)^2]^{-1}$. The change is largely discernible in the shifts in the frequency bands at which pairs of various flexural aliasing orders cross; the shifts are to higher frequencies. Otherwise the influence of the change on patterns of the aliased modal drive $\bar{P}_{sn}(k, \omega)$ is insignificant, notwithstanding that the cancellations are weaker

and narrower at the crossings of pairs of various flexural aliasing orders as the ring impedance of the ribs is diminished, by definition, at the higher frequency ranges. Figure 5a is repeated in Fig. 5e, except that the mode index (n) is changed from the standard value of unity to zero. The absence of the shear free waves in Fig. 5e is consistent with Fig. 3e.

The first sub-figures in the fifth and sixth sets; i.e., Figs. 6a and 7a, are computed under standard parametric values. The patterns in the normalized modal response $\bar{V}_n(k, \omega)$ manifest footprints of the aliasing in the normalized drive $\bar{P}_{sn}(k, \omega)$. However, since neither the term $\bar{P}_{en}(k, \omega)$ [$= \exp(ix_a k)$] nor the factor $\bar{G}_{\infty n}(k, \omega)$, in Eqs. (13) and (14), are aliased in (k) with respect to (κ_1) , the aliasing in $\bar{P}_{sn}(k, \omega)$ is spoiled in $\bar{V}_n(k, \omega)$; the quantity $\bar{V}_n(k, \omega)$ is not strictly aliased. The “ribs’ free term” $\bar{V}_{\infty n}(k, \omega)$ in this quantity accentuates and reemphasizes the zeroth order patterns and the factor $\bar{G}_{\infty n}(k, \omega)$ in the “ribs’ term” $\bar{V}_{sn}(k, \omega)$ subdues the aliased patterns in $\bar{P}_{sn}(k, \omega)$ once $[(ak)^2 + (n/a)^2] > (k_{po})^2$ is satisfied. The subduing increases the more this inequality is satisfied. The first of these effects is manifested in that the patterns in Figs. 2a and 3a, are, respectively, overlaid in Figs. 4a and 5a. The second is manifested in that the patterns in Figs. 4a and 5a are suppressed in Figs. 6a and 7a in spectral ranges that lie beyond the flexural free waves. The second effect is made clearer in Figs. 6a.1 and 7a.1. These figures are the clipped version of Figs. 6a and 7a, respectively; values that lie below a given threshold in Figs. 6a and 7a are removed in Figs. 6a.1 and 7a.1 [2,3]. For the sake of completeness Figs. 6a and 7a are repeated in Figs. 6b-d and 7b-e, with changes that correspond to those made in Figs. 4b-d and 5b-e with respect to Figs. 4a and 5a, respectively. The features in the patterns of Figs. 6a and 7a drawn from the patterns in Figs. 2a and 4a and 3a and 5a, respectively, can be generalized to the other sub-figures in these categories; e.g., the patterns in Fig. 7c are overlaid of patterns in Fig. 3c and of patterns in Fig. 5c. The patterns in the latter figure are, however, subdued in spectral ranges that lie beyond the flexural free waves. Thus, changes in the

parametric values and accompanied influences in Figs. 2 through 5, if correspondingly selected, impose similar influences in Figs. 6 and 7.

The derivation and manipulation of the modal response $\bar{V}_n(k, \omega)$ and its composition are found to be relatively simple in the k -domain. The algebraic nature of the modal response $\bar{V}_{\infty n}(k, \omega)$ induced by the normalized modal external drive $\bar{P}_{en}(k, \omega)$ in the absence of the ribs, the harmonic nature of the drive $\bar{P}_{sn}(k, \omega)$ in lieu of the ribs and, again, the algebraic nature of the modal response $\bar{V}_{sn}(k, \omega)$ induced by this drive, render efficacious the k -domain for formulating the modal response $\bar{V}_n(k, \omega)$. The descriptions of this quantity and terms and factors in its composition are presented in Figs. 2 through 7. These descriptions demonstrate that the flexural free waves are the dominant response contributors, that the fluid free waves are weak contributors even when fluid loading is heavy and, finally, although the membrane free waves are discernible and they are evidently scattered by the ribs, the membrane free waves are nonetheless weak contributors to the response, especially at the higher frequency range, where $(2\omega_r / \omega_c) \leq (\omega / \omega_c)$. In Figs. 2f and 3f and g the flexural free waves are substantially weakened by increasing the flexural loss factor (η_p) by more than an order of magnitude. The other free waves remain substantially unaltered so that they are relatively accentuated. The quantitative assessments of the weakening of the flexural free waves and the accentuation, thereby, of the other free waves are not readily afforded by Figs. 2 and 3 which include Figs. 2f and 3f and g. In this light, can a Fourier transformation of $\bar{V}_{\infty n}(k, \omega)$ into the x -domain assist in these assessments?

III. MODAL RESPONSE OF A UNIFORM CYLINDER IN THE SPATIAL DOMAIN

The expression for the normalized modal response $\bar{V}_{\infty n}(k, \omega)$ of a uniform cylinder is stated in Eq. (13a). As already observed, neither the term $\exp(ix_a k)$ nor the factor $\bar{G}_{\infty n}(k, \omega)$ are aliased and, therefore, the modal response $\bar{V}_{\infty n}(k, \omega)$ in the k -domain is not aliased. The Fourier transformation of $\bar{V}_{\infty n}(k, \omega)$ into the spatial x -domain affords no factorial saving performing the transformation either via Eq. (1-10b) or via Eq. (1-14); indeed, computations of this kind are relatively simple. Nonetheless, to obtain compatibility and in preparation for performing computations that are more compounded, the technique described in Eq. (1-14) is utilized to Fourier transform $\bar{V}_{\infty n}(k, \omega)$ to $\bar{v}_{\infty n}(x, \omega)$. From Eqs. (1-14) and (13a), and after an appropriate normalization, one obtains

$$\bar{v}_{\infty n}(x, \omega) \simeq$$

$$e_n(\omega) [\kappa_1(1+R)^{-1}] \sum_{r=0}^R S_b^J(k_r) \{ \bar{G}_{\infty n}(k_r, \omega) \exp[-i(x - x_a)k_r] \} ;$$

$$e_n(\omega) = [(2/\pi^2 k_{po}^2) \{(n/ak_{po})^4 - 1\}]^{1/2} ; \quad (-1)^{1/2} = (-i) . \quad (16)$$

The normalization adopted in Eq. (16) yields for a hybrid cylinder in the absence of fluid loading, at the position of the external ring drive; i.e., at $(|x - x_a|/b) = 0$, a unit amplitude. In Fig. 8a the normalized modal response $\bar{v}_{\infty n}(x, \omega)$ is displayed as a function of (x/b) for the normalized frequency $(\omega/\omega_c) = 0.175$. The computations in this figure are performed under standard parametric values for a hybrid cylinder. Computations pertaining to changes in the fluid loading parameter (ε_c) from the standard value of 10^{-2} to 10^{-4} and 10^{-1} are superposed on the original Fig. 8a. [cf. Figs. 2a-c.] The influence of the fluid surface mass loading is revealed in this figure;

the curves pertaining to $\varepsilon_c = 10^{-2}$ and 10^{-4} substantially overlap, whereas the curve for $\varepsilon_c = 10^{-1}$ lies just below, but consistently adjacent. There is, however, no evidence of fluid free waves in Fig. 8a; the dominance of the flexural free waves appear overwhelming. This figure is repeated in Figs. 9a and 10a, except that a natural cylinder is substituted for the hybrid cylinder and the mode index (n) is selected to be unity and zero, respectively. Figures 9a and 10a are identical to Fig. 8a and, therefore, it appears that the dominance of the flexural free waves overwhelms not only the fluid free waves, but also the membrane free waves. To emphasize this identity, Fig. 8a is jointly designated Figs. 9a and 10a. Can the flexural free waves be rendered weak enough so that those other types of free waves, which are faintly, but clearly discernible in Fig. 2 and 3, may be boldly exposed and investigated? Figures 2f and 3f and g suggest that damping the flexural free waves may induce the desired weakening in these free waves. Figures 8a, 9a and 10a are repeated in Figs. 8b, 9b and 10b, respectively, except that the flexural loss factor (η_p) is changed from the standard value of 10^{-3} to 3×10^{-2} , a substantial increase in damping. This increase in damping of the flexural free waves appears more dramatic and revealing in Figs. 8b, 9b and 10b than in the corresponding Figs. 2d, 3d and 3g in the k -domain. In Figs. 8b, 9b and 10b the increase spatial decay of the flexural free waves is bottomed; this bottoming is not due to lack of computational accuracy, but, rather, due to the existence and presence of other types of free waves. In part, to help substantiate this statement Figs. 8c, 9c and 10c are added. In these figures the fluid loading parameter (ε_c) is set equal to 10^{-6} and, in conformity, the flexural loss factor (η_p) is retained equal to 3×10^{-2} . Figures 8c, 9c and 10c are also superposed on Figs. 8b, 9b and 10b. The presence of fluid free waves emerges in Fig. 8b and the presence of fluid and membrane free waves emerge in Figs. 9b and 10b. Moreover, manifestation of interferences among the various types of free waves are discernible in these figures. Interferences occur in "regions" in which more than one type of free waves are present with strengths within an order of magnitude. Thus, in

Figs. 8b and c interference occurs in the region of the bottoming knee; this interference is between the flexural and fluid free waves. In this region the strengths of these two types of free waves are within an order of magnitude. Increasing the spatial distance ($|x - x_a|/b$) beyond the knee, leaves the fluid free waves alone; the flexural free waves are weakened out by the high damping. Changes in the strength of the fluid free waves are then exhibited in Fig. 8b; the knees appropriately adjust to these changes over several orders of magnitude. In passing it is recalled that in Fig. 8a the fluid loading significantly influences the surface impedance of the cylinder only when $\varepsilon_c > 10^{-2}$. Indeed, this influence causes the saturation and reversal in the strength of fluid free waves as the fluid loading parameter (ε_c) is increased through 10^{-2} on to 10^{-1} . The apparent anomaly is associated with Le Chatlier's principle [2]. In Figs. 9b and c and 10b and c, the membrane free waves join in; in Figs. 9b and c the membrane free waves are comprised of two components; longitudinal and shear free waves and in Figs. 10b and c of one component; longitudinal free waves only. These differences in the two sets of figures help decipher the free waves that are involved in the interferences. For example, it is clear from Figs. 9c and 10c that the strengths of the longitudinal and shear free waves, at $(\omega/\omega_c) = 0.175$, are within an order of magnitude and, therefore they significantly interfere in Fig. 9c, whereas this interference is absent in Fig. 10c. In these two figures the fluid free waves do not participate in the interference; the fluid free waves are rendered weak by selecting the fluid loading parameter (ε_c) equal to 10^{-6} in these figures. Clearly the fluid free waves participate in the interferences depicted in Figs. 9b and 10b for a fluid loading parameter $\varepsilon_c \geq 10^{-2}$; in particular with the membrane free waves at distances ($|x - x_a|/b$) beyond the bottoming knees. The details that are captured in the interferences in these figures attest to the accuracy attained in the computations via Eq. (1-14). The simplicity of the summand and, therefore, the simplicity of the computations performed to generate Figs. 8 through 10, may not convincingly constitute a critical proof of the viability of Eq. (1-14).

Nonetheless, the kind of figures just presented are of intrinsic value, especially as they relate and assist in deciphering figures displaying more compounded computations; those that account for the attachment of ribs on the cylinder.

IV. MODAL DRIVE IN LIEU OF THE RIBS IN THE SPATIAL DOMAIN

The normalized modal drive $\bar{P}_{sn}(k, \omega)$ in lieu of the ribs is typically depicted in the k -domain for a hybrid and a natural cylinder in Figs. 4 and 5, respectively. These figures are computed under standard parametric values and for a selected variety in these values. These figures demonstrate that this quantity is aliased in (k) with respect to (κ_1) ; the expression for this quantity in Eq. (14) confirms this aliasing. Moreover, the expression for $\bar{P}_{sn}(k, \omega)$ indicates that Eq. (1-21) suitability befits the formula for performing the Fourier transformation for this quantity. Designating $\bar{p}_{sn}(x, \omega)$ the Fourier transform of $\bar{P}_{sn}(k, \omega)$, Eqs. (1-14), (1-21) - (1-23) and (14) are used to derive

$$\begin{aligned}\bar{p}_{sn}(x, \omega) &= s_b(x) \{ \delta(x) \bar{p}_{sn}^o(x, \omega) \} ; \\ \bar{p}_{sn}(x, \omega) &= [p_s(x, \omega) / P_{en}^o(\omega)] ,\end{aligned}\quad (17)$$

where

$$\begin{aligned}\bar{p}_{sn}^o(x, \omega) &\simeq \\ (1+R)^{-1} \sum_{r=0}^R \exp(-ixk_r) &I_{bn}^J(k_r, \omega) S_b^J(k_r) \{ Q_{\infty n}(k_r, \omega) \exp(ix_a k_r) \} ,\end{aligned}\quad (18a)$$

$$I_{bn}^J(k, \omega) = [1 + S_b^J(k) Q_{\infty n}(k, \omega)]^{-1} , \quad (18b)$$

and it is recognized that in Eqs. (17) and (18) there exist a factorial saving of $(2J+1)^2$ in computational steps as compared with estimating $\bar{p}_{sn}(x, \omega)$ from $\bar{P}_{sn}(k, \omega)$ employing the discrete Fourier transform procedure, as stated in Eq. (1-2c). The absolute values of

$\bar{p}_{sn}^o(x, \omega)$ as a function of the normalized frequency (ω / ω_c) for a hybrid and a natural cylinder are presented in Figs. 11 and 12, respectively. The computations are performed for $(x / b) \Rightarrow (x_j / b) = 7, 14, 21$ and 35 and for a mode index (n) equal to unity. Each of these figures is composed of three values of the fluid loading parameter; namely, $\varepsilon_c = 10^{-4}, 10^{-2}$ and 10^{-1} . The presence of the phenomenon of pass and stop bands with respect to the flexural free waves emerges in these figures. The influence of fluid loading on this phenomenon is also distinguished in these figures. In particular there is a shift to lower frequencies of the stop bands with increase in fluid loading; the shift is more pronounced the higher the fluid loading is. This shift in frequencies is related to the added surface mass component in the fluid surface impedance as already discussed with respect to Figs. 2-5. This and other complemental features in $\bar{P}_{sn}(k, \omega)$ and $\bar{p}_{sn}^o(x, \omega)$ are facilitated by superimposing the corresponding computations performed on each quantity in the same figure. Thus, Figs. 4 and 5 simultaneously exhibit both quantities. It is observed in these figures that the high spatial decay in the modal drive $\bar{p}_{sn}^o(x, \omega)$ in a (flexural) stop band in the x -domain, is appropriately commensurate with the uniformity in the drive $\bar{P}_{sn}(k, \omega)$ in a stop band in the k -domain. This uniformity is derived from cancellations between pairs of flexural dispersive aliasing orders in those spectral regions in which they cross. In the absence of these cancellations, as is the case in a first order model in which interactions among the ribs via the cylindrical shell are neglected, pass and stop bands are also absent [2,13]. The pass and stop bands are largely dominated by the flexural free waves; the other types of free waves are poorly manifested by a few minor kinks in the curves depicting $\bar{p}_{sn}^o(x, \omega)$ and a few corresponding kinks in the curves depicting $\bar{P}_{sn}(k, \omega)$. Other features in these quantities can be similarly related from the k -domain to the x -domain and vice versa; e.g., the shifts in frequencies of the stop bands due to a change in the character of the ring impedance of the ribs from mass to stiffness controlled correctly track in the complemental representations in Figs. 4d and 5d. There are, of course,

features that are more indigenous to one domain than another. The aliasing in $\bar{P}_{sn}(k, \omega)$ are clearly a k -domain phenomenon. On the other hand, in a stop band, when the distance $(|x_j - x_a|/b)$ exceeds a specific value, the decay in $\bar{p}_{sn}^o(x, \omega)$ is bottomed. The bottomings in the (flexural) stop bands are clearly a x -domain phenomenon. The bottoming phenomenon in a stop band is reminiscent of the same named phenomenon induced by the increase in damping of the flexural free waves in the absence of ribs. Is there a commonality in these two phenomena?

V. RESPONSE OF A REGULARLY RIBBED CYLINDER IN THE SPATIAL DOMAIN

The normalized modal response $\bar{V}_n(k, \omega)$ is composed of two terms, $\bar{V}_{\infty n}(k, \omega)$ and $\bar{V}_{sn}(k, \omega)$, as stated in Eqs. (12) and (13). Formally, from Eqs. (1-1a), (12) and (13) one obtains

$$\bar{v}_n(x, \omega) = \bar{v}_{\infty n}(x, \omega) - \bar{v}_{sn}(x, \omega), \quad (19)$$

$$\bar{v}_{\infty n}(x, \omega) = e_n(\omega) (2\pi)^{-1/2} \int dk \exp(-ixk) \bar{V}_{\infty n}(k, \omega), \quad (20a)$$

$$\bar{v}_{sn}(x, \omega) = e_n(\omega) (2\pi)^{-1/2} \int dk \exp(-ixk) \bar{V}_{sn}(k, \omega), \quad (20b)$$

where $e_n(\omega)$ is the normalization factor defined in Eq. (16). The Fourier transform of the first term is dealt with in Section III; in this section the second term is added to the computational task. As already discussed in the k -domain, neither $\bar{V}_{\infty n}(k, \omega)$ nor $\bar{V}_{sn}(k, \omega)$ are strictly aliased. In the first term neither of its two factors are aliased and, therefore, no factorial saving can be accrued from the form of its evaluation. In the second term the factor $\bar{G}_{\infty n}(k, \omega)$ is not aliased; however, the second factor, being the modal drive $\bar{P}_{sn}(k, \omega)$ in lieu of the ribs, is aliased. Identifying $\bar{G}(k, \omega)$ as $\bar{G}_{\infty n}(k, \omega)$ and $K(k, \omega)$ as $\bar{P}_{sn}(k, \omega)$ in Eq. (1-14), and with Eqs. (1-16b) and (14a) in tow, a factorial saving of $(2J+1)$, and with Eqs. (1-19b) and (14b) in tow, a factorial saving of $(2J+1)^2$ of computational steps may be accrued in the evaluation of $\bar{v}_{sn}(x, \omega)$ in Eq. (20b). [This kind of saving is not afforded using Eq. (1-2c).] From Eqs. (1-14), (1-19b), (14b) and (20b) one obtains

$$\bar{v}_{sn}(x, \omega) \approx$$

$$e_n(\omega) [\kappa_1(1+R)^{-1}] \sum_{r=0}^R I_n^J(k_r, \omega) S_b^J(k_r) \{Q_{\infty n}(k_r, \omega) \exp(ix_a k_r)\} \\ S_b^J(k_r) \{\exp(-ixk_r) \bar{G}_{\infty n}(k_r, \omega)\};$$

$$e_n(\omega) = [(2/\pi^2 k_{po}^2) \{(n/ak_{po})^4 - 1\}]^{1/2}; \quad (-1)^{1/2} = (-i). \quad (21)$$

The normalization and evaluation of the second term in Eq. (19) are rendered compatible, in Eq. (21), with those of the first term in Eq. (16). A question may be raised: Since the aliasings phenomenon in $\bar{P}_{sn}(k, \omega)$ is spoiled in $\bar{V}_n(k, \omega)$ and the pass and stop bands phenomenon is revealed in the modal drive $\bar{p}_{sn}(x, \omega)$, is the pass and stop bands phenomenon spoiled in the modal response $\bar{v}_n(x, \omega)$? In other words, how akin are these two phenomena? The absolute value of the normalized modal response $\bar{v}_n(x, \omega)$ is displayed as a function of (x/b) , for a hybrid cylinder in Fig. 13 and a natural cylinder in Figs. 14 and 15; in Figs. 14 and 15 the mode index is set equal to unity and zero, respectively. In Figs. 13a, 14a and 15a the frequency is set at $(\omega/\omega_c) = 0.175$ with the fluid loading parameter $\epsilon_c = 10^{-6}, 10^{-4}, 10^{-2}$ and 10^{-1} and at $(\omega/\omega_c) = 0.158$ with $\epsilon_c = 10^{-1}$. It is observed that data pertaining to the frequency $(\omega/\omega_c) = 0.175$ with $\epsilon_c = 10^{-6}, 10^{-4}$, and 10^{-2} and the frequency $(\omega/\omega_c) = 0.158$ with $\epsilon_c = 10^{-1}$ lie in a (flexural) stop band. The data pertaining to a frequency $(\omega/\omega_c) = 0.175$ with $\epsilon_c = 10^{-1}$ substantially lie in a pass band; the shift in the frequencies of the stop bands under the influence of heavy fluid loading accounts for this feature in the data with respect to $\epsilon_c = 10^{-1}$. [cf. Figs. 11 and 12.] Figures 13a, 14a and 15a convincingly indicate that the pass and stop bands phenomenon is not closely akin to the phenomenon of aliasing; the spoiling of the aliasing in $\bar{V}_n(k, \omega)$ does not entail the

spoiling of the pass and stop bands in $\bar{v}_n(x, \omega)$. It emerges, however, that data in Figs. 13a, 14a and 15a that lie in the stop band at $(\omega/\omega_c) = 0.175$ with $\varepsilon_c = 10^{-6}$, 10^{-4} and 10^{-2} and at $(\omega/\omega_c) = 0.158$ with $\varepsilon_c = 10^{-1}$, are reminiscent of the corresponding data in Figs. 8b, 9b and 10b, respectively. This reminiscence holds even with respect to the reversal of strength between the fluid free waves with $\varepsilon_c = 10^{-2}$ and 10^{-1} ; the anomaly is particularly discernible in Figs. 8b and 13a. In the vein of Figs. 8c, 9c and 10c, the curves in Figs. 13a, 14a and 15a that pertain to a fluid loading parameter $\varepsilon_c = 10^{-6}$ are, in isolation, displayed in Figs. 13b, 14b and 15b, respectively. Notwithstanding that there exist minor and accountable differences in levels, the resemblance between Figs. 13a and b, 14a and b, and 15a and b and Figs. 8b and c, 9b and c, and 10b and c, respectively, is striking. The resemblance even matches the bottoming and interference phenomena described earlier. Indeed, comparison among the correspond figures in the two sets leads one to conclude that the regularly attached ribs in a stop band play a role that is commensurate with the role played by the increase in flexural damping in the absence of ribs. This conclusion does not take account of the undulations in level within a bay that exist in the former set, but are absent in the latter set of figures [14]. The undulations are avoided in the former set of figures by an appropriate selection of the position (x_a/b) of the external drive and the regularity of the sampling positions (x/b) along the axis of the cylinder [14]. These undulations are not significant enough, however, to altercate the striking resemblance between these two sets of figures.

Figures 13a and b, 14a and b, and 15a and b are made possible only with an accuracy and a reproductive details that transcend several orders of magnitude. In the computations that underlie these figures the overall wavenumber span (k_M) and the sampling wavenumber span (κ_1) are related largely by a $J = 50$, yielding a factorial saving of 10^2 and, in some cases, of 10^4 of computational steps in computations performed with the double-sum technique versus computations performed with

techniques that are directly akin to the discrete Fourier transform procedures. Whether this kind of factorial savings is crucial to the generation of the figures presented in this report is a matter of memory and patience. The former can be bought and the latter can be acquired by practice, notwithstanding that shortages on both accounts are thinning out. Nonetheless, that the double-sum technique has been successfully employed to furnish the figures just presented is by now a fact.

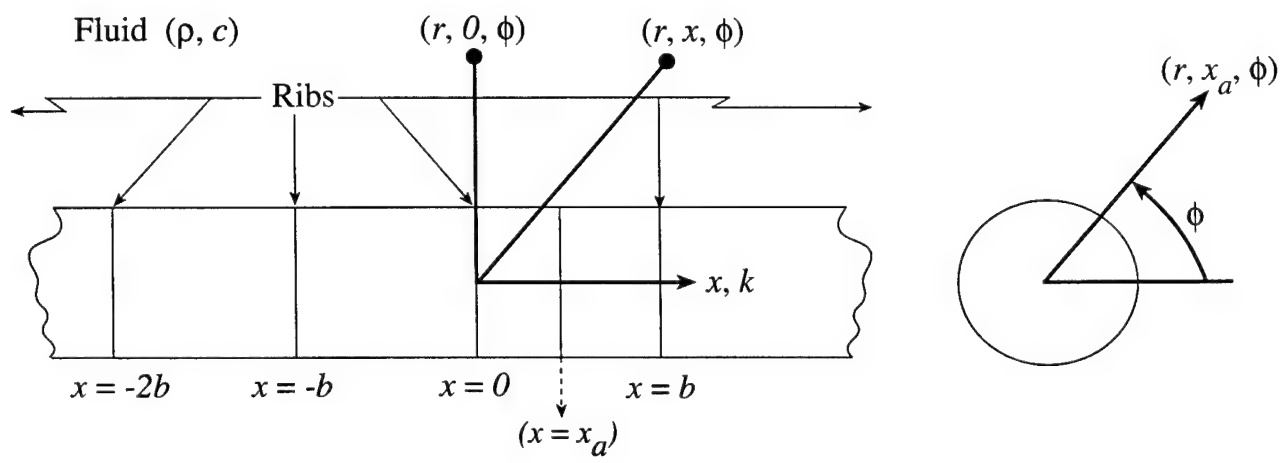


Fig. 1. A sketch of a regularly ribbed cylinder and coordinate system.

Fig. 2. Normalized modal response $\bar{V}_{\infty n}(k, \omega)$ of

a uniform **hybrid** cylinder as a function of

the normalized axial wavenumber (ak) in

a frequency waterfall format.

a. Under standard values. [cf. Eq. (15).]

- b. $\varepsilon_c = 10^{-4}$.
- c. $\varepsilon_c = 10^{-1}$.
- d. $\eta_p = 3 \times 10^{-2}$.
- e. $n = 0$.

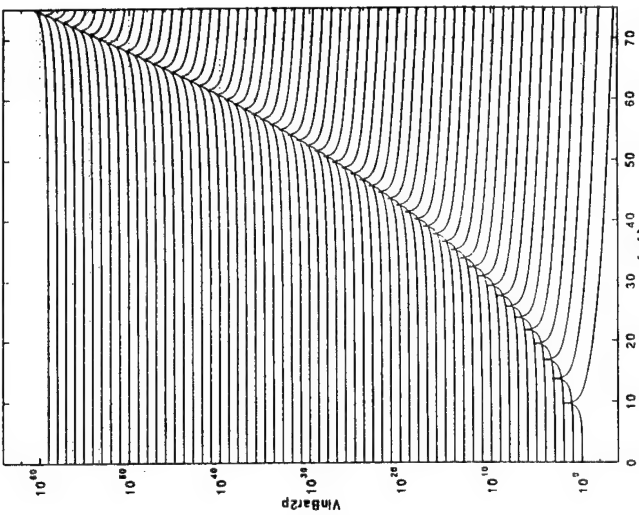


Fig. 2a

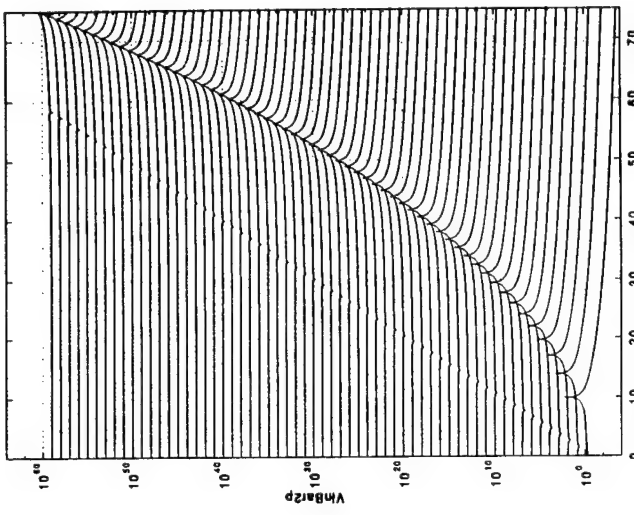


Fig. 2b

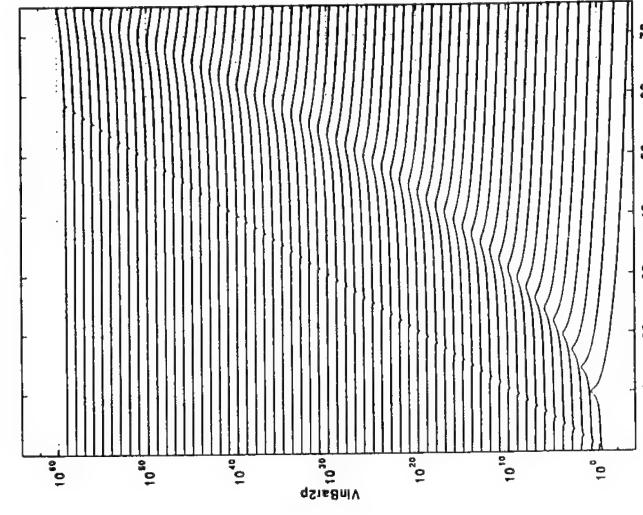


Fig. 2c

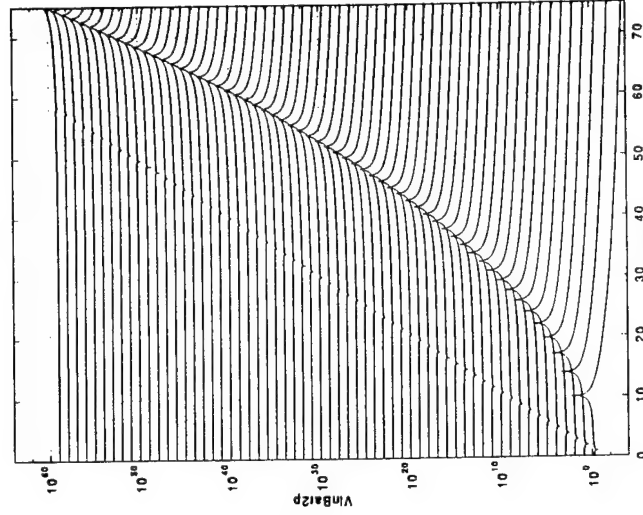


Fig. 2d

Fig. 3. As Fig. 2 but for a natural cylinder.

- a. Under standard values. [cf. Eq. (15).]
- b. $\varepsilon_c = 10^{-4}$.
- c. $\varepsilon_c = 10^{-1}$.
- d. $\eta_p = 3 \times 10^{-2}$.
- e. $n = 0$.
- f. $n = 2$.
- g. $n = 0$ and $\eta_p = 3 \times 10^{-2}$.

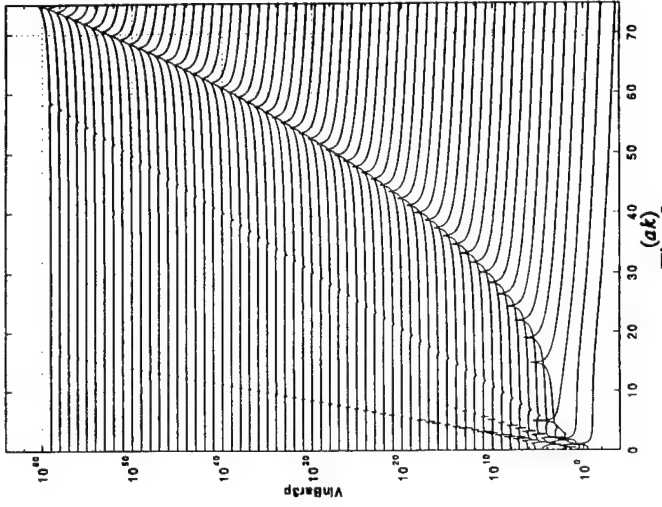


Fig. 3a

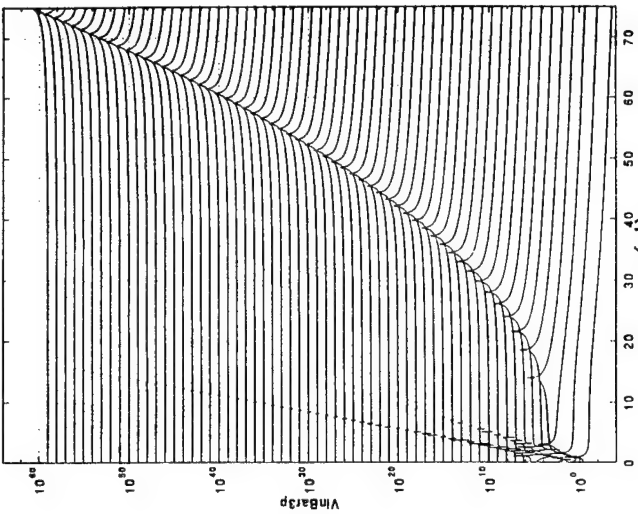


Fig. 3b

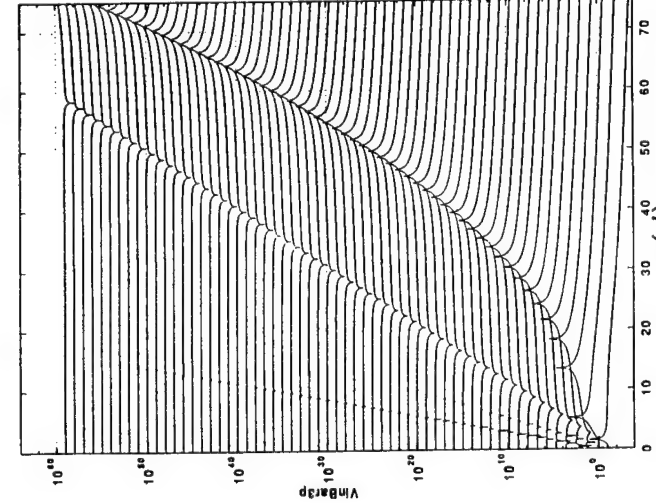


Fig. 3c

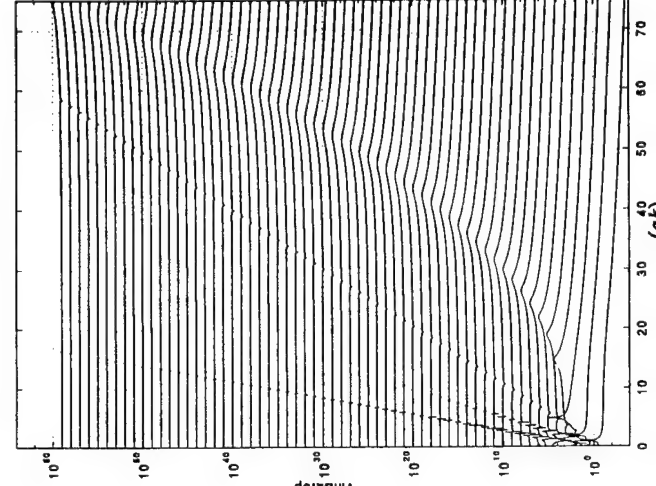


Fig. 3d

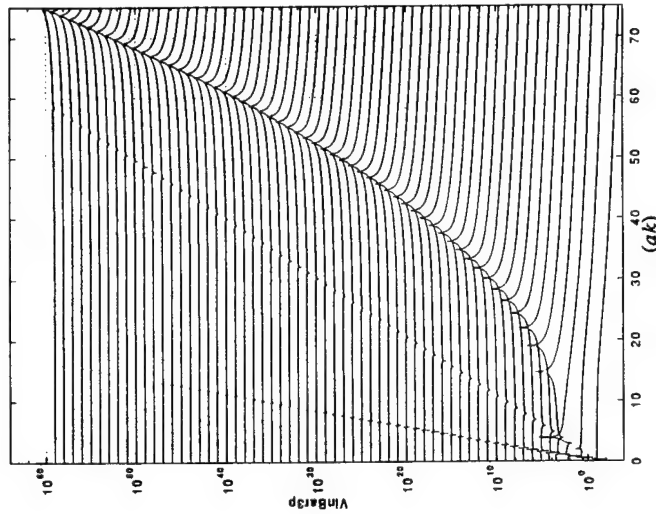


Fig. 3e

Fig. 4. Normalized modal drive $\bar{P}_{sn}(k, \omega)$ in lieu of the ribs on a **hybrid** cylinder as a function of the normalized axial wavenumber (ak) in a frequency waterfall format. Superposed is the normalized modal drive $\bar{p}_{sn}(x, \omega)$ in lieu of the ribs for a **hybrid** cylinder as a function of the normalized frequency (ω / ω_c) for the normalized axial distances (x/b) = 7, 14, 21 and 35.

a. Under standard values. [cf. Eq. (15).]
 b. $(x_a/b) = 0.3$.
 c. $\varepsilon_c = 10^{-1}$.
 d. Ribs' ring impedance stiffness controlled.

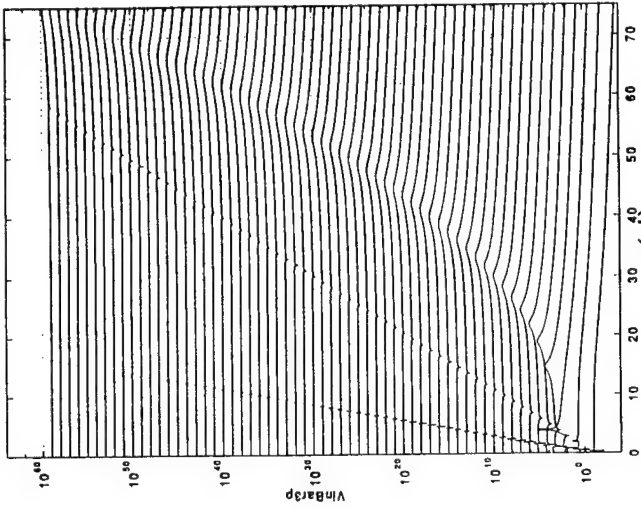


Fig. 3g

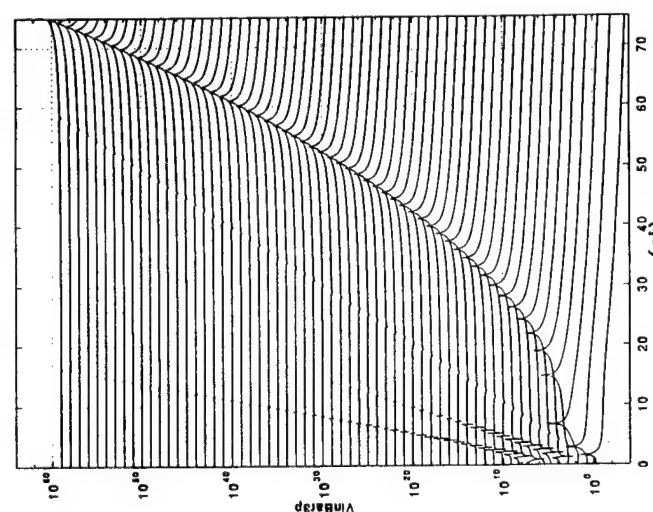


Fig. 3f

35

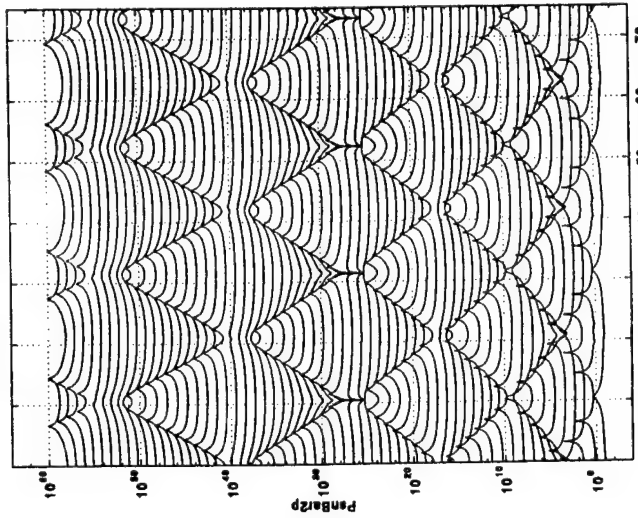


Fig. 4b

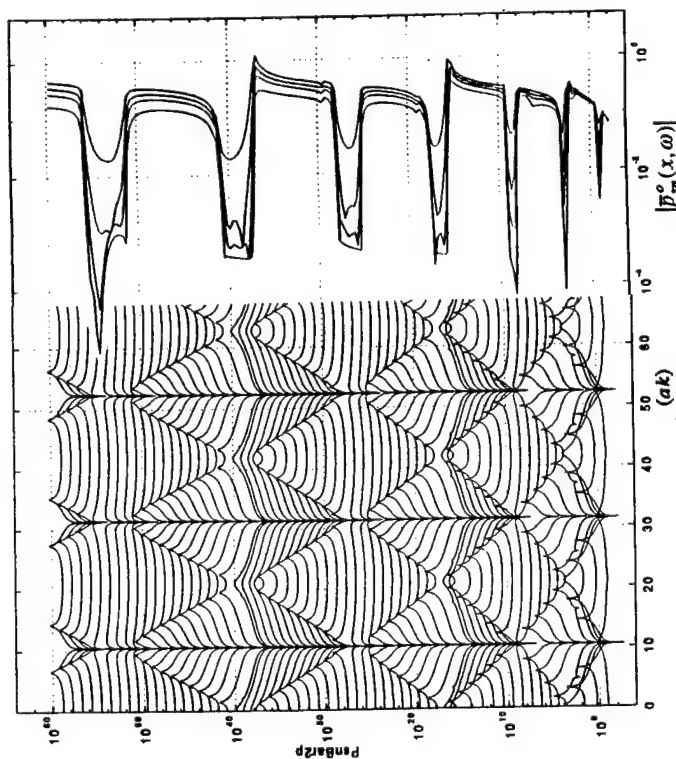


Fig. 4a

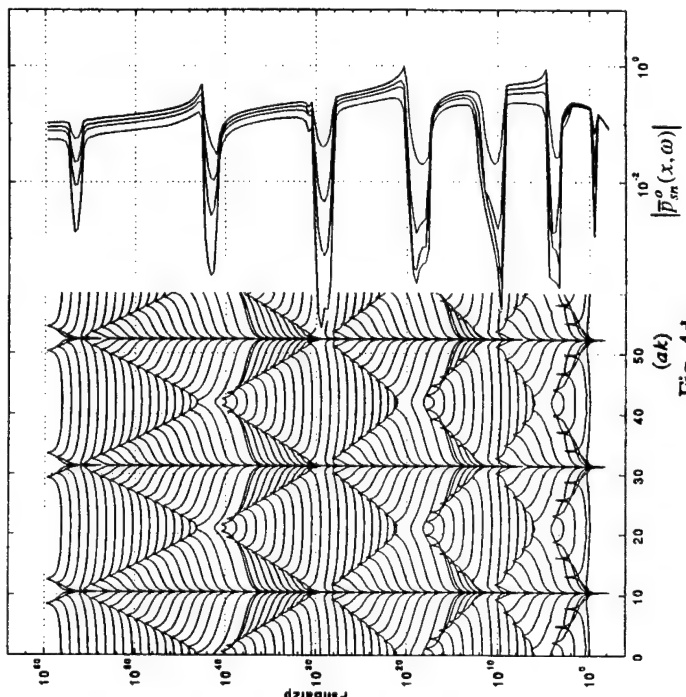


Fig. 4d

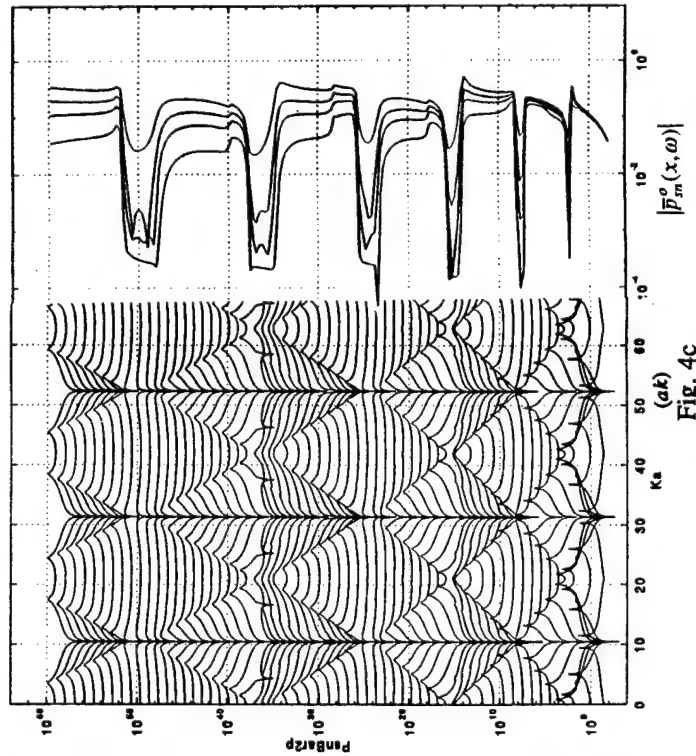


Fig. 4c

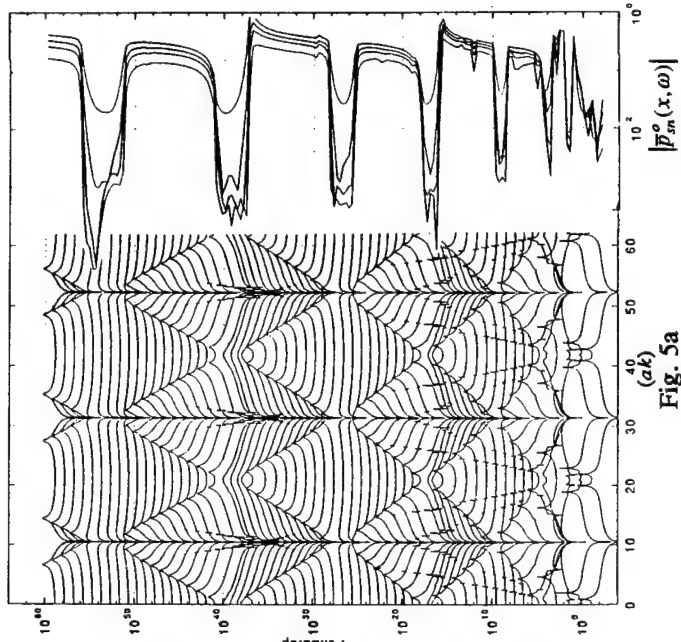


Fig. 5a

Fig. 5. As Fig. 4 but for a natural cylinder.

- a. Under standard values. [cf. Eq. (15).]
- b. $(x_a/b) = 0.3$.
- c. $\varepsilon_c = 10^{-1}$.
- d. Ribs' ring impedance stiffness controlled.
- e. $n = 0$.

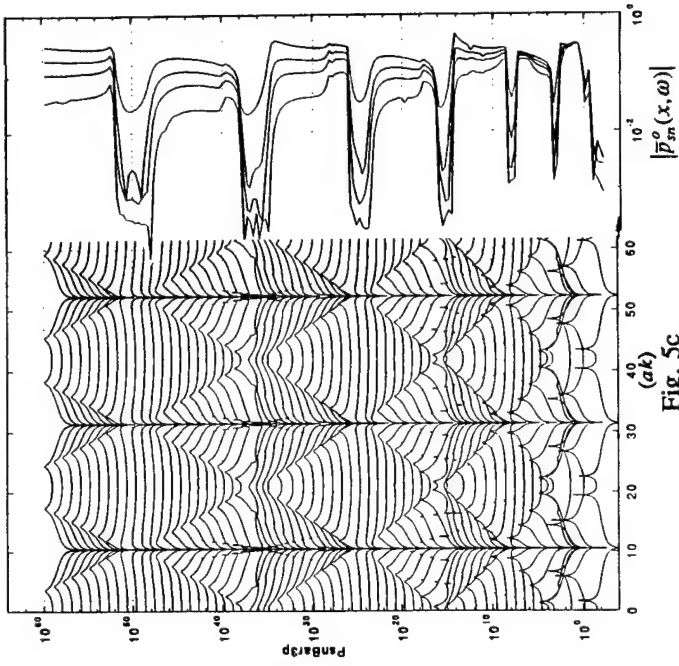


Fig. 5c

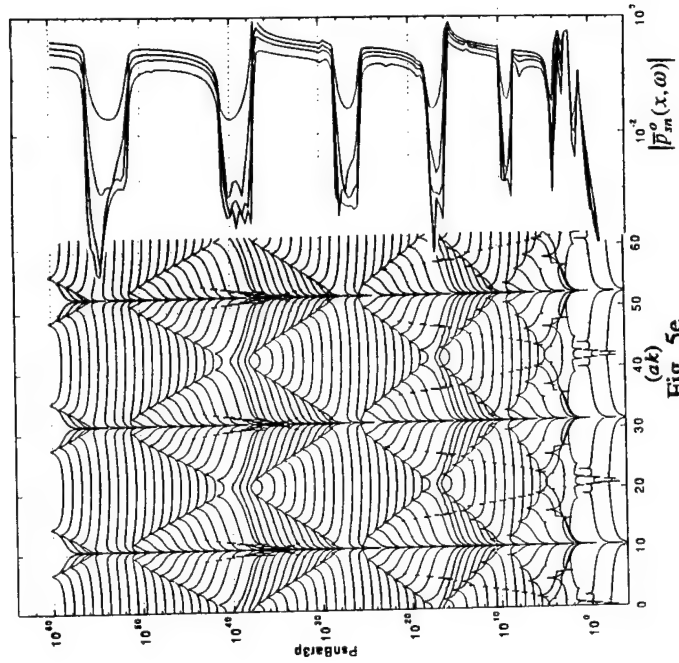


Fig. 5d

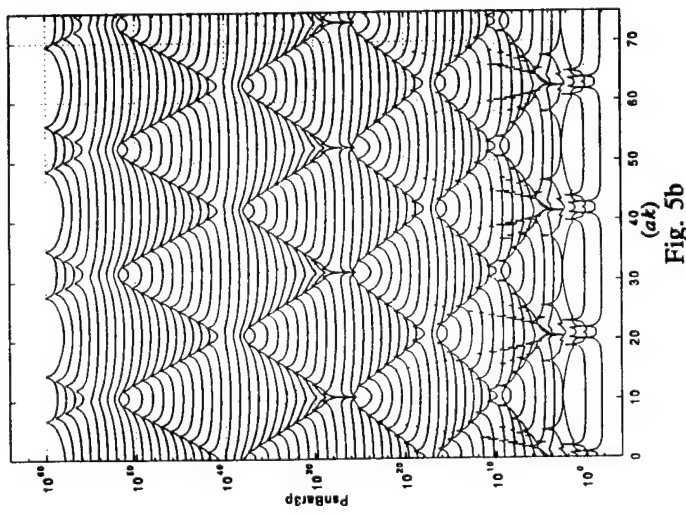


Fig. 5b

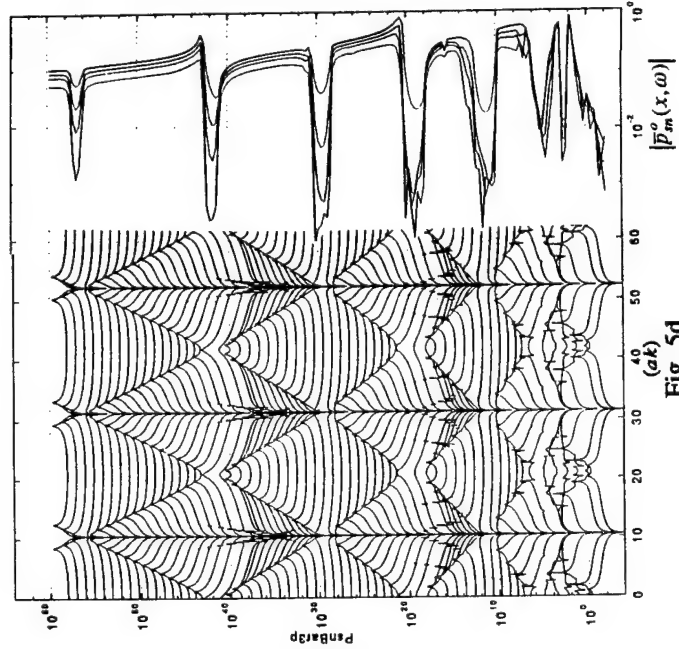


Fig. 5e

Fig. 6. Normalized response $\bar{V}_n(k, \omega)$ of a regularly ribbed hybrid cylinder as a function of the normalized axial wavenumber (ak) in a frequency waterfall format.

- a. Under standard values. [cf. Eq. (15).]
- a.1. Clipping of Fig. 6.a.
- b. $\epsilon_c = 10^{-4}$.
- c. $\epsilon_c = 10^{-1}$.
- d. Ribs' ring impedance stiffness controlled.
- e. $n = 0$.

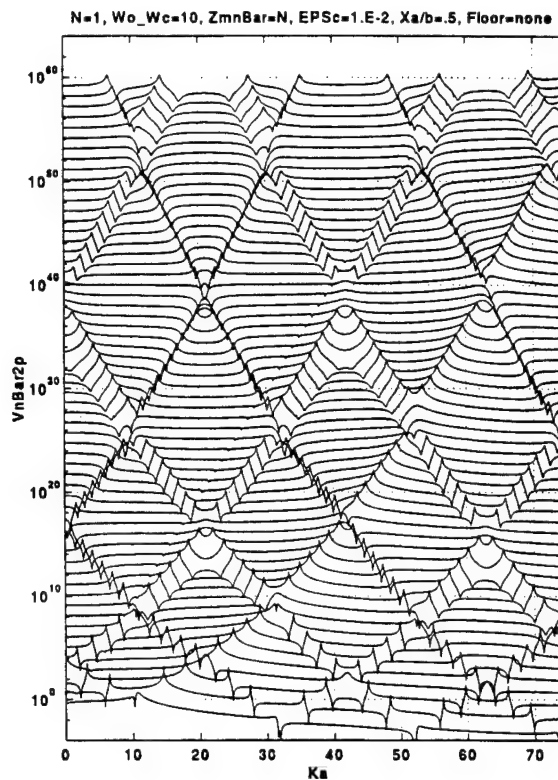


Fig. 6a

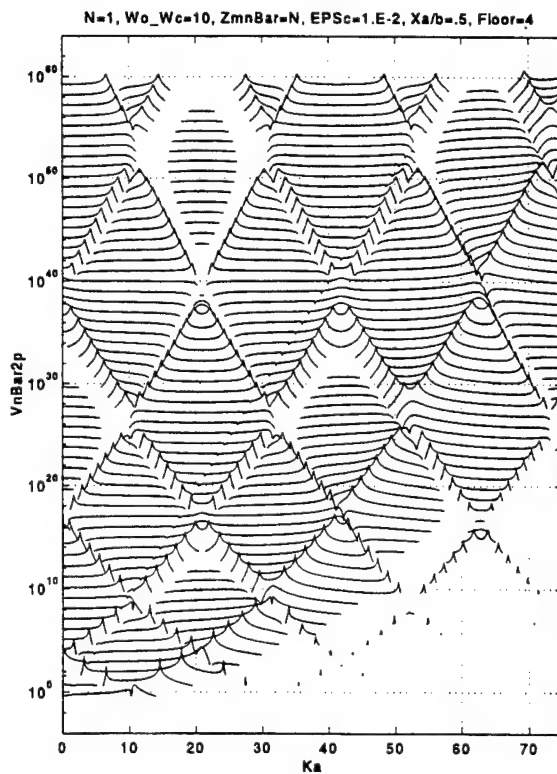


Fig. 6al

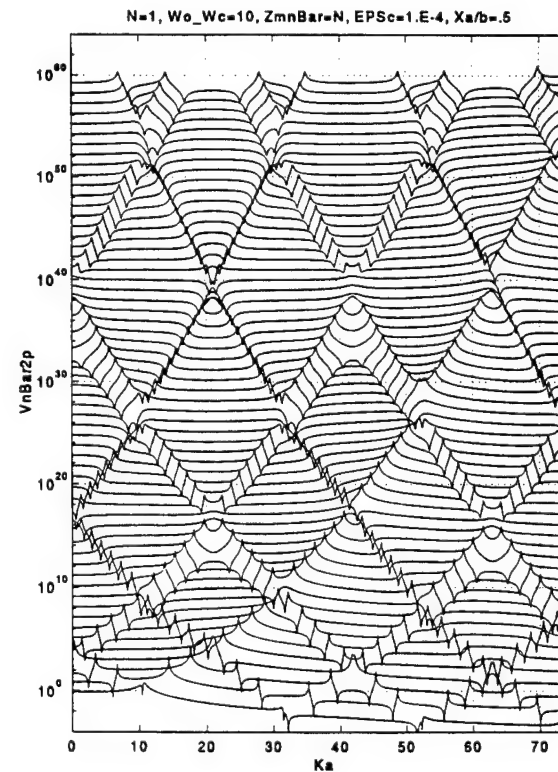


Fig. 6b

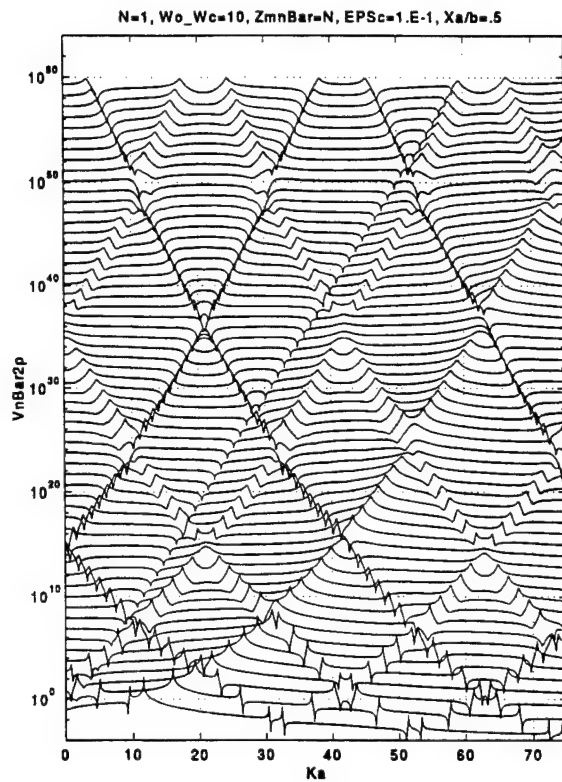


Fig. 6c

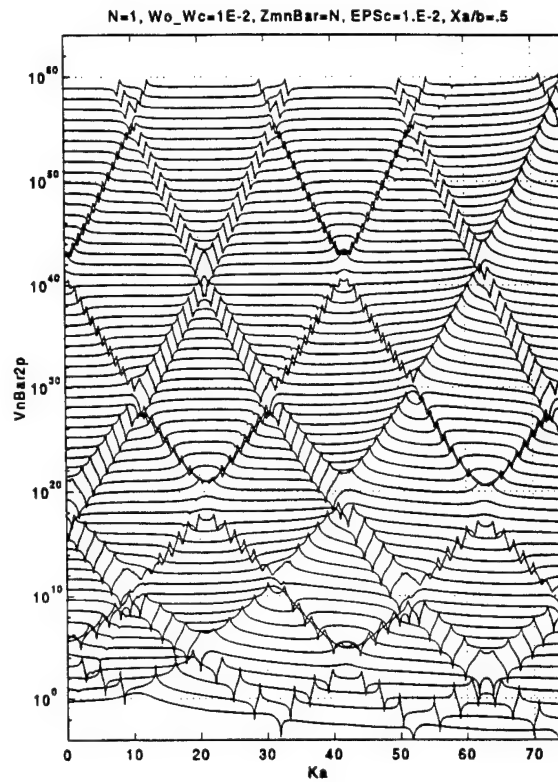


Fig. 6d

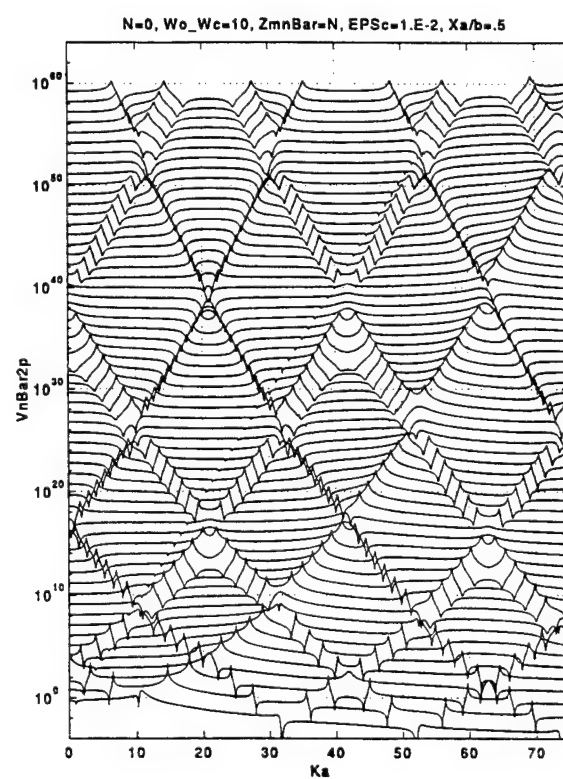


Fig. 6e

Fig. 7. As Fig. 6 but for a natural cylinder.

- a. Under standard values. [cf. Eq. (15).]
- a.1. Clipping of Fig. 7.a.
- b. $\varepsilon_c = 10^{-4}$.
- c. $\varepsilon_c = 10^{-1}$.
- d. Ribs' ring impedance stiffness controlled.
- e. $n = 0$.

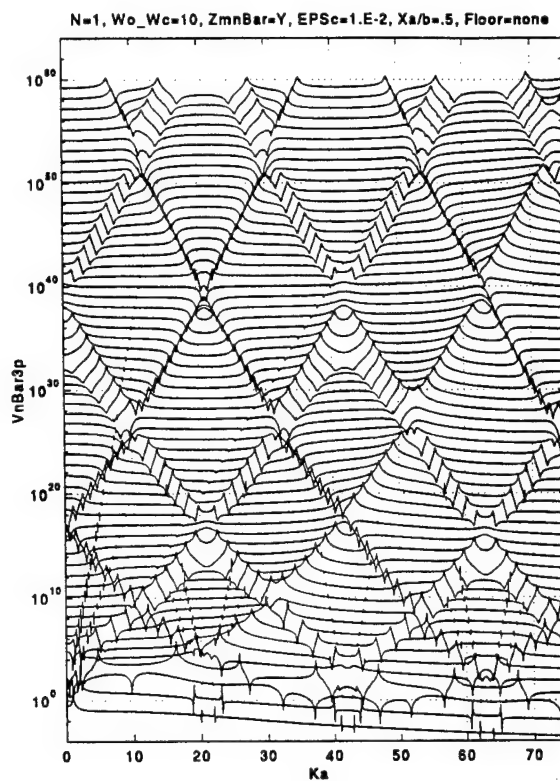


Fig. 7a

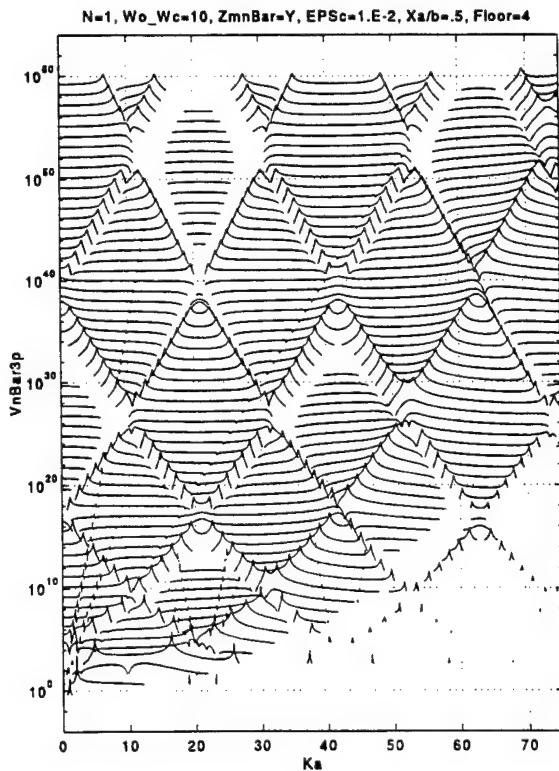


Fig. 7al

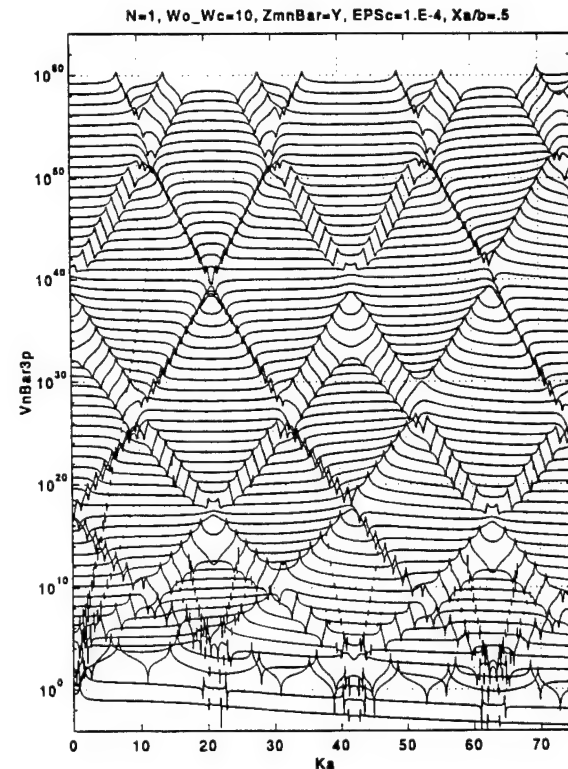


Fig. 7b

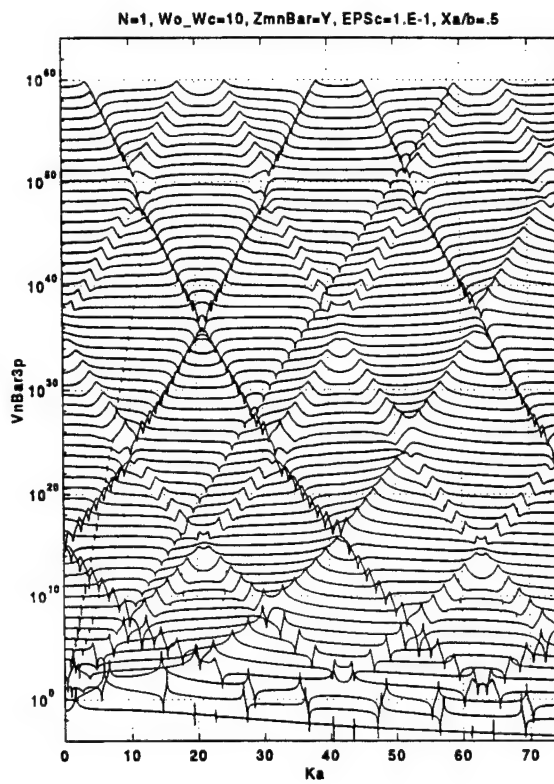


Fig. 7c

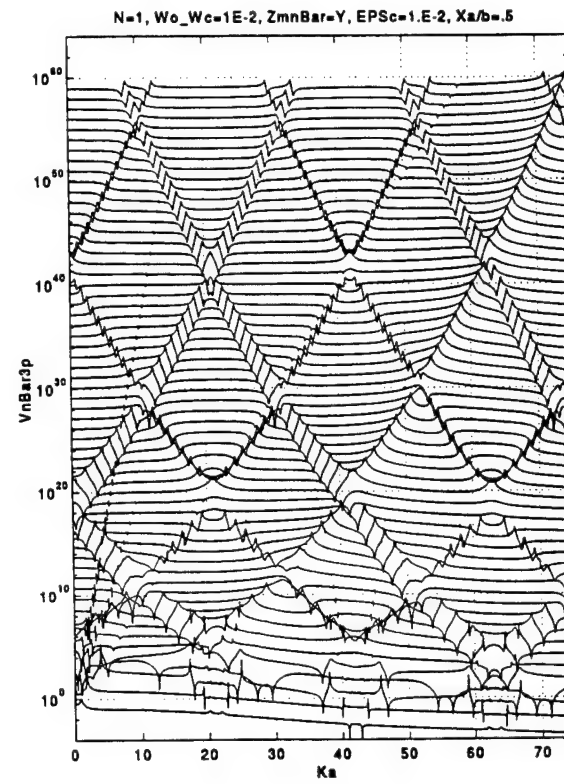


Fig. 7d

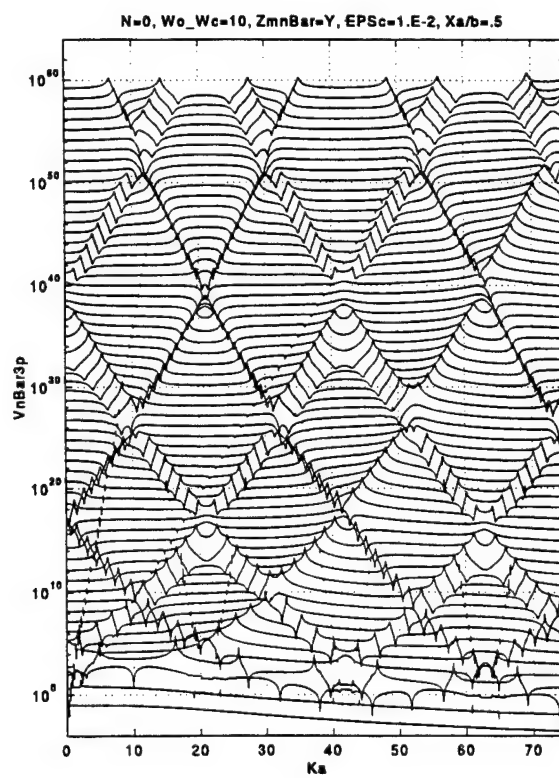
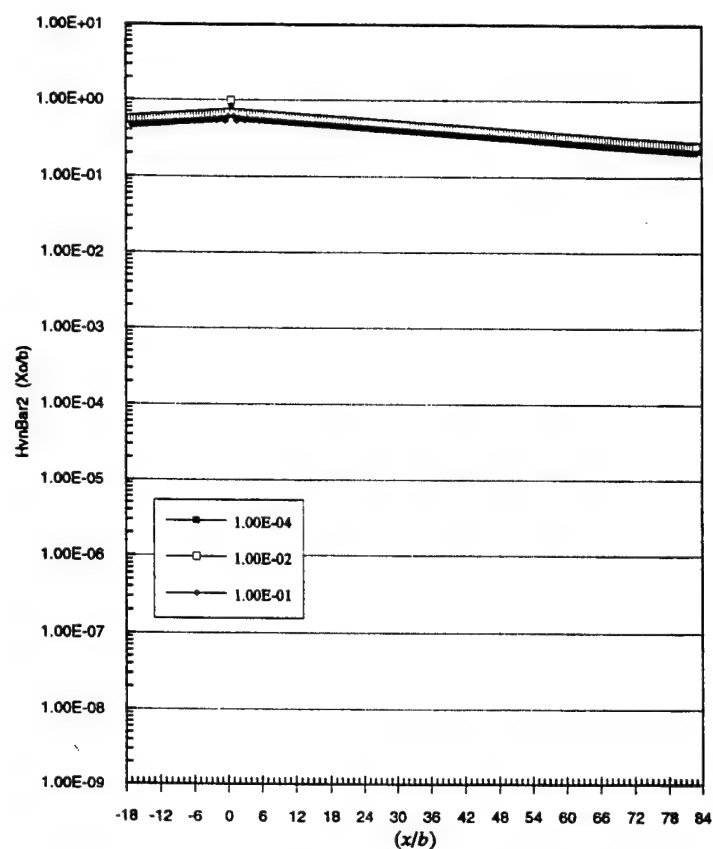


Fig. 7e

Fig. 8. Normalized modal response $\bar{v}_{\infty n}(x, \omega)$ of a uniform hybrid cylinder as a function of the normalized axial distance (x/b) at the normalized frequency $(\omega/\omega_c) = 0.175$.

- a. Under standard values and for $\varepsilon_c = 10^{-4}, 10^{-2}$ and 10^{-1} .
- b. $\eta_p = 3 \times 10^{-2}$ and $\varepsilon_c = 10^{-6}, 10^{-4}, 10^{-2}$ and 10^{-1} .
- c. $\eta_p = 3 \times 10^{-2}$ and $\varepsilon_c = 10^{-6}$.



Figs. 8a, 9a, and 10a

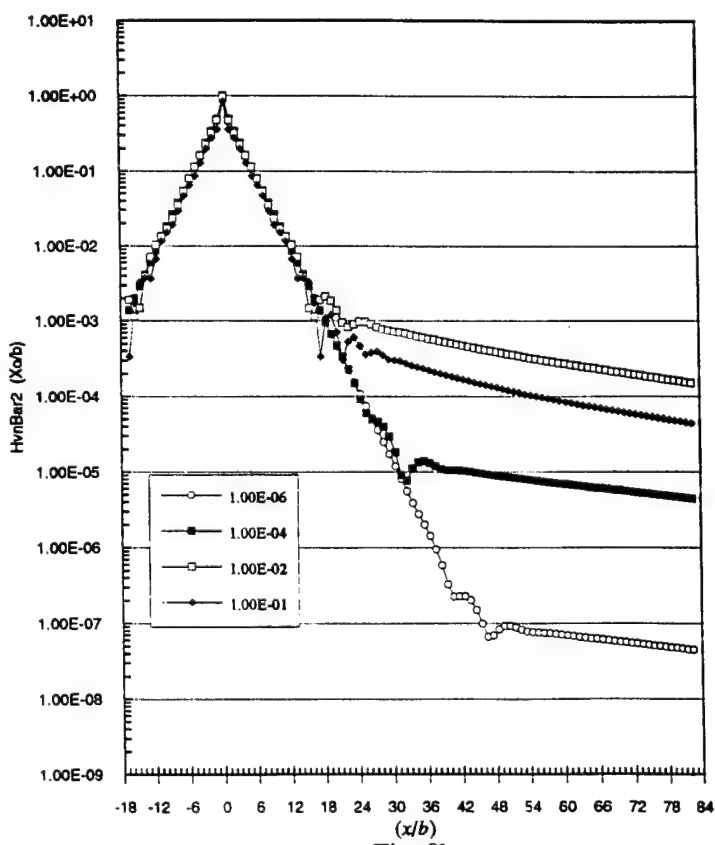


Fig. 8b

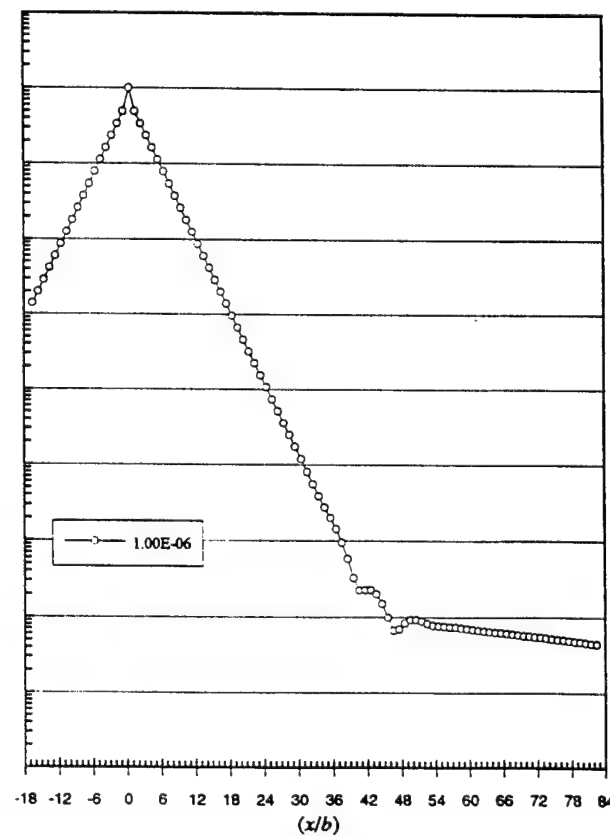
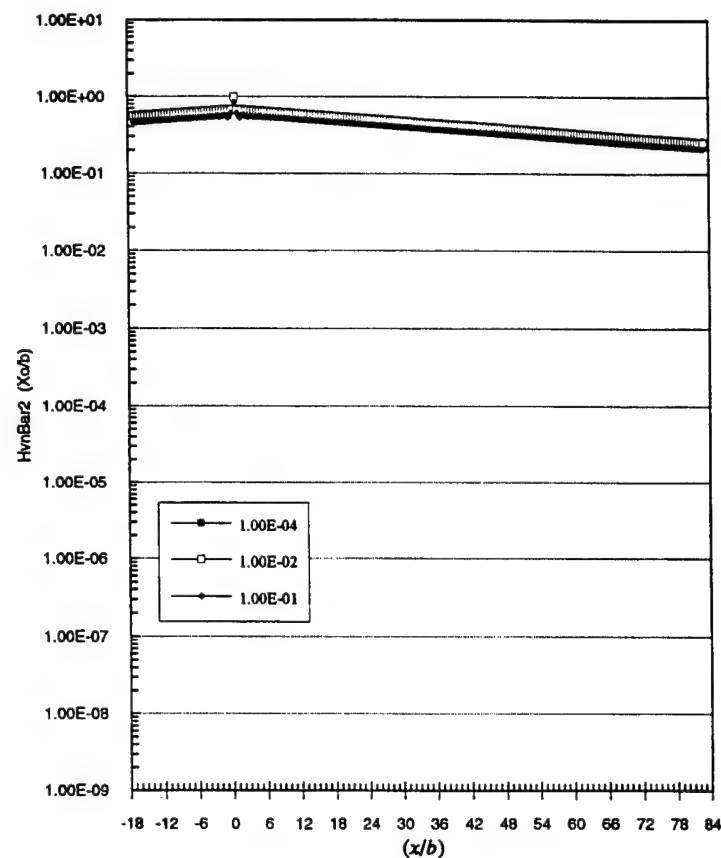


Fig. 8c

Fig. 9. As Fig. 8 but for a natural cylinder.

- a. Under standard values and for $\epsilon_c = 10^{-4}, 10^{-2}$ and 10^{-1} .
- b. $\eta_p = 3 \times 10^{-2}$ and $\epsilon_c = 10^{-6}, 10^{-4}, 10^{-2}$ and 10^{-1} .
- c. $\eta_p = 3 \times 10^{-2}$ and $\epsilon_c = 10^{-6}$.



Figs. 8a, 9a, and 10a (Repeated)

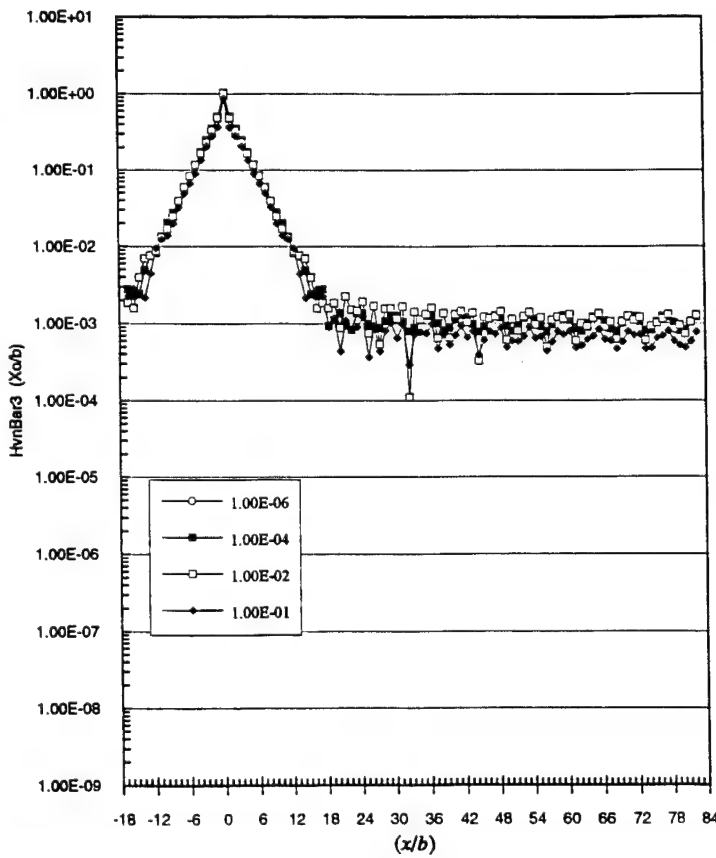


Fig. 9b

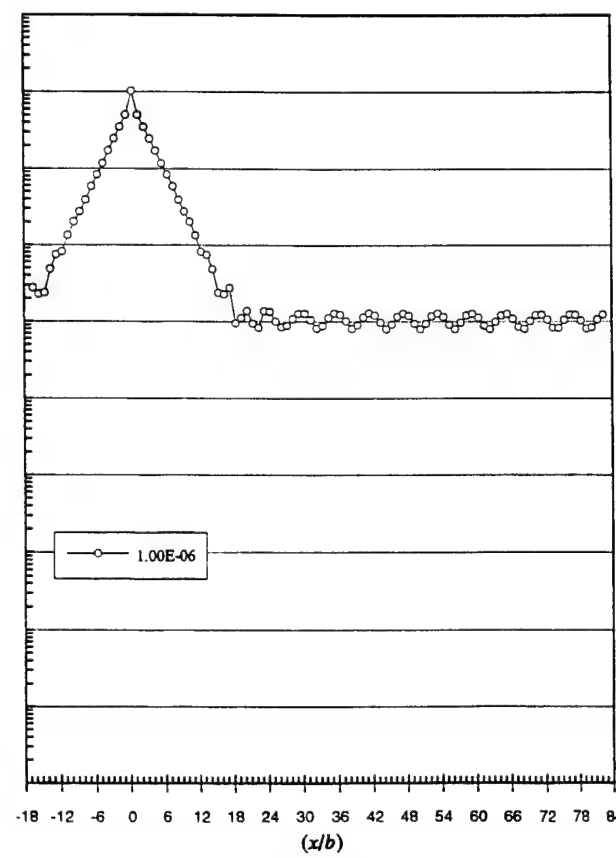
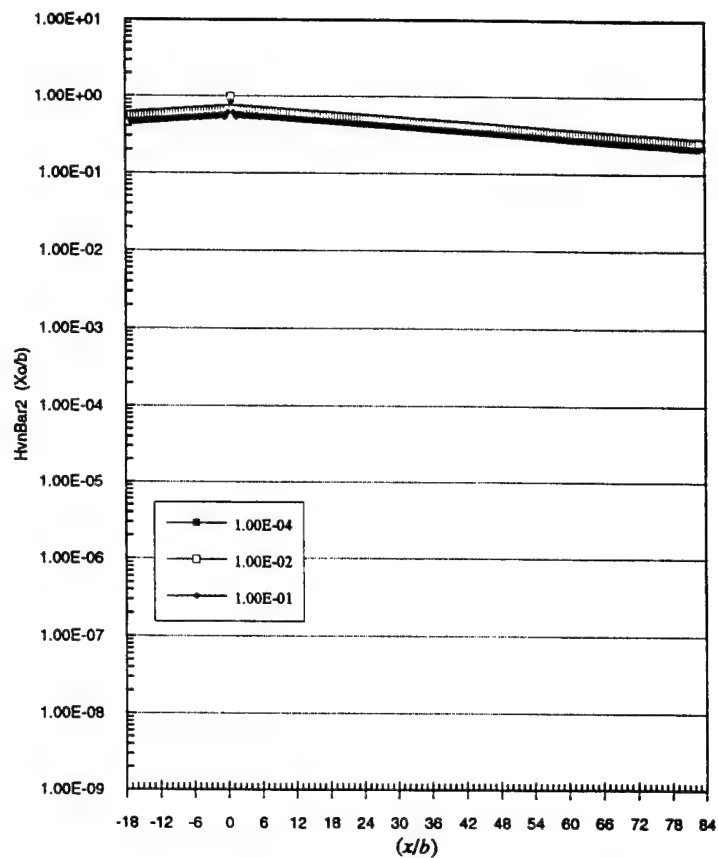


Fig. 9c

Fig. 10. As Fig. 9 except (n) is changed from the standard value of unity to zero.

- a. $\varepsilon_c = 10^{-4}, 10^{-2}$ and 10^{-1} .
- b. $\eta_p = 3 \times 10^{-2}$ and $\varepsilon_c = 10^{-6}, 10^{-4}, 10^{-2}$ and 10^{-1} .
- c. $\eta_p = 3 \times 10^{-2}$ and $\varepsilon_c = 10^{-6}$.



Figs. 8a, 9a, and 10a (Repeated)

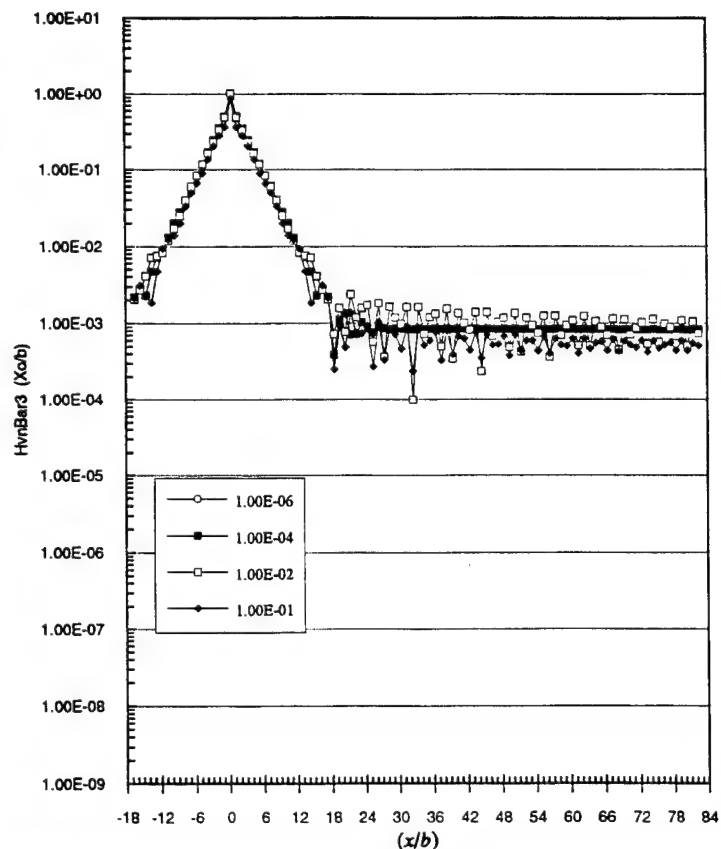


Fig. 10b

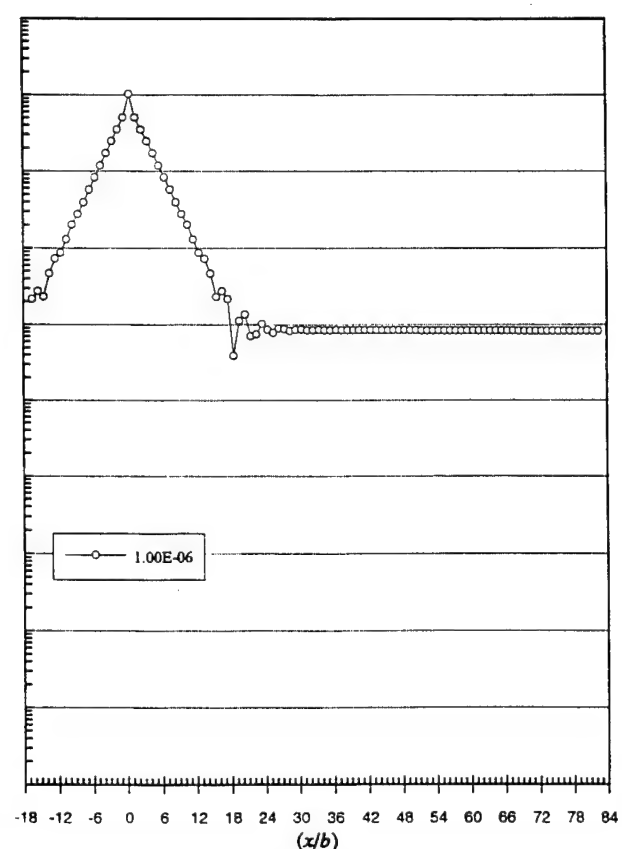


Fig. 10c

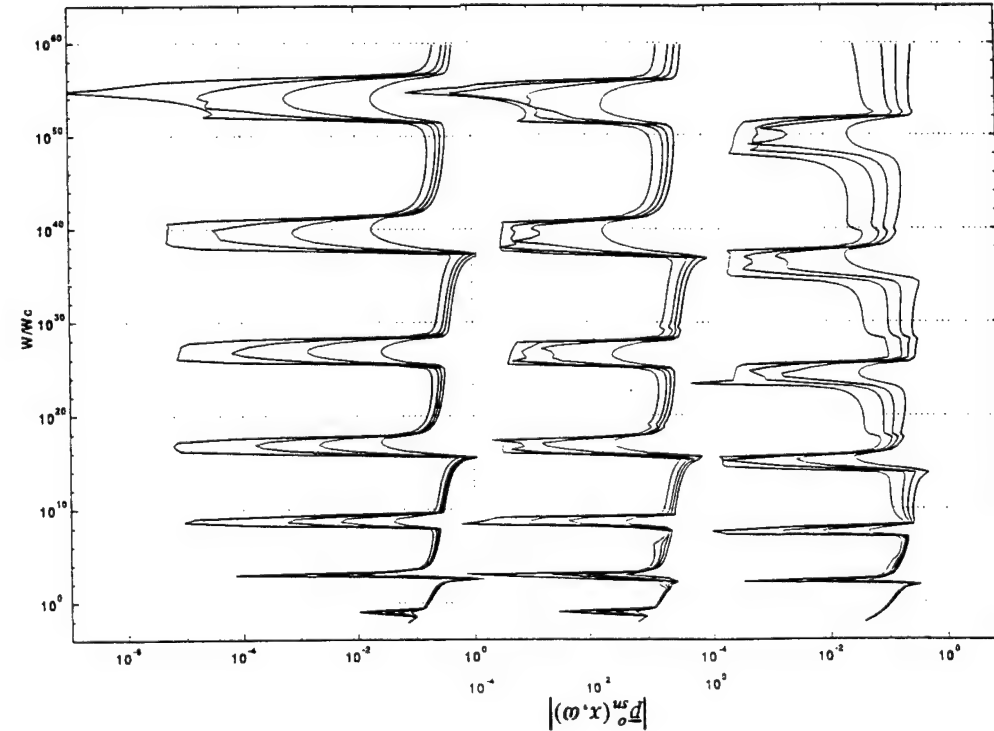
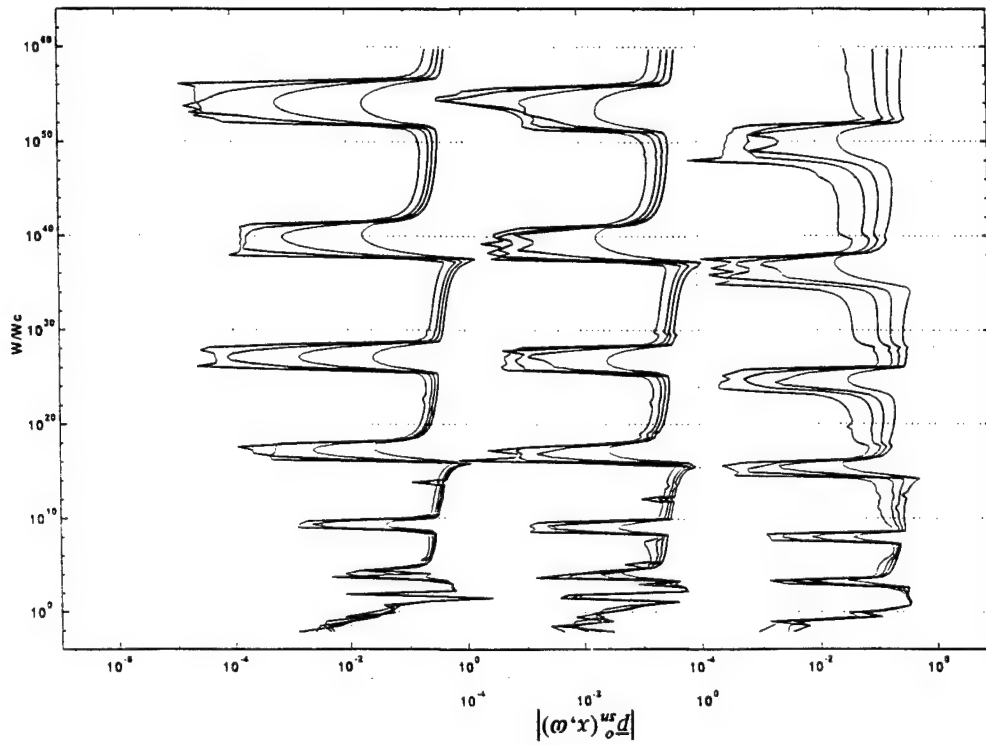


Fig. 12. As Fig. 11 but for a natural cylinder.

Fig. 11. Normalized modal drive $\bar{p}_{sn}(x, \omega)$ in lieu of the ribs on a **hybrid** cylinder as a function of the normalized frequency (ω / ω_c) for the normalized axial distances $(x / b) = 7, 14, 21$ and 35 and for $\varepsilon_c = 10^{-4}$, $\varepsilon_c = 10^{-2}$ and 10^{-1} .

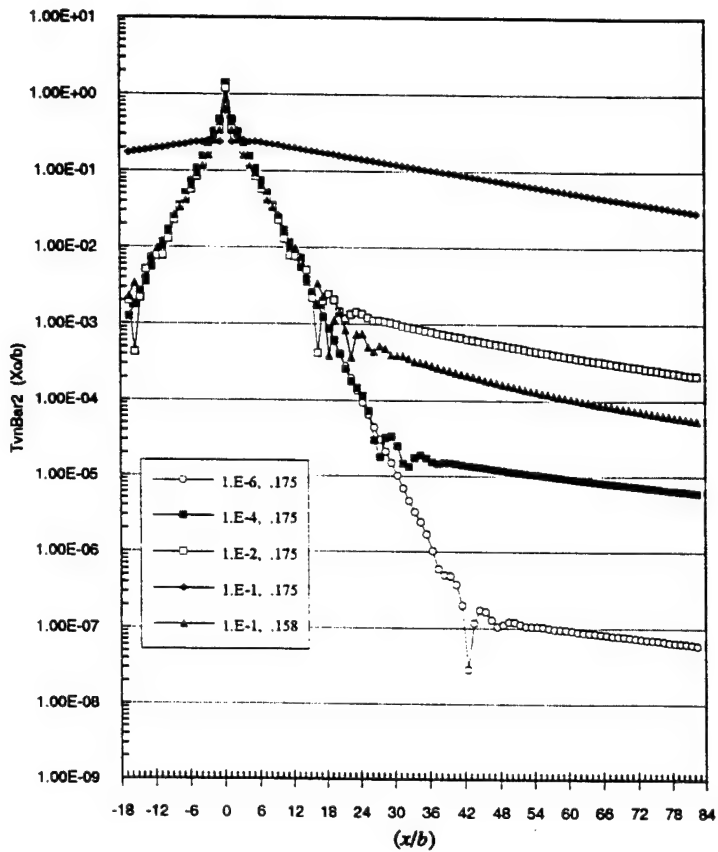


Fig. 13a

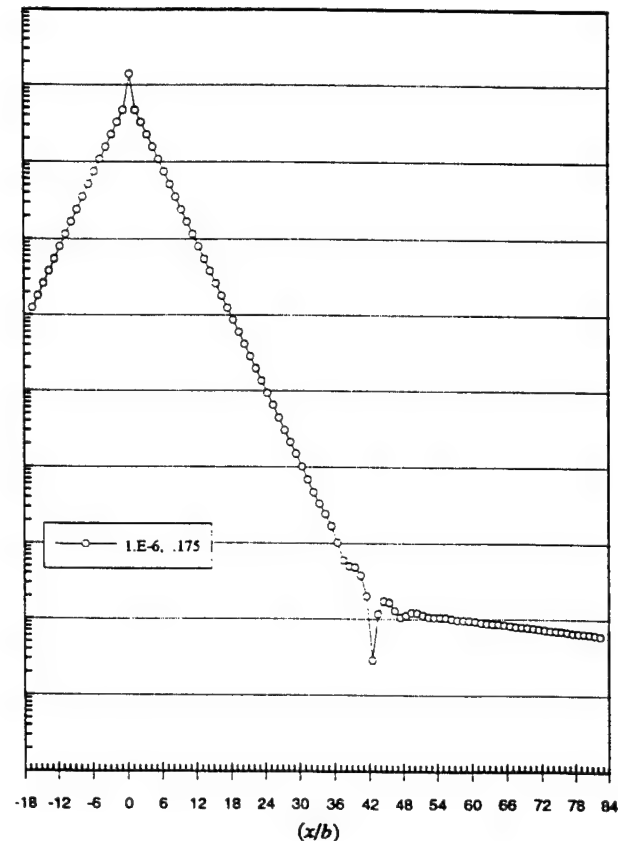


Fig. 13b

Fig. 13. Normalized modal response $\bar{v}_n(x, \omega)$ of a regularly ribbed **hybrid** cylinder as a function of the normalized axial distance (x/b) .

- a. $(\omega/\omega_c) = 0.175$ with $\varepsilon_c = 10^{-6}, 10^{-4}, 10^{-2}$ and 10^{-1} and $(\omega/\omega_c) = 0.158$ with $\varepsilon_c = 10^{-1}$.
- b. $(\omega/\omega_c) = 0.175$ with $\varepsilon_c = 10^{-6}$.

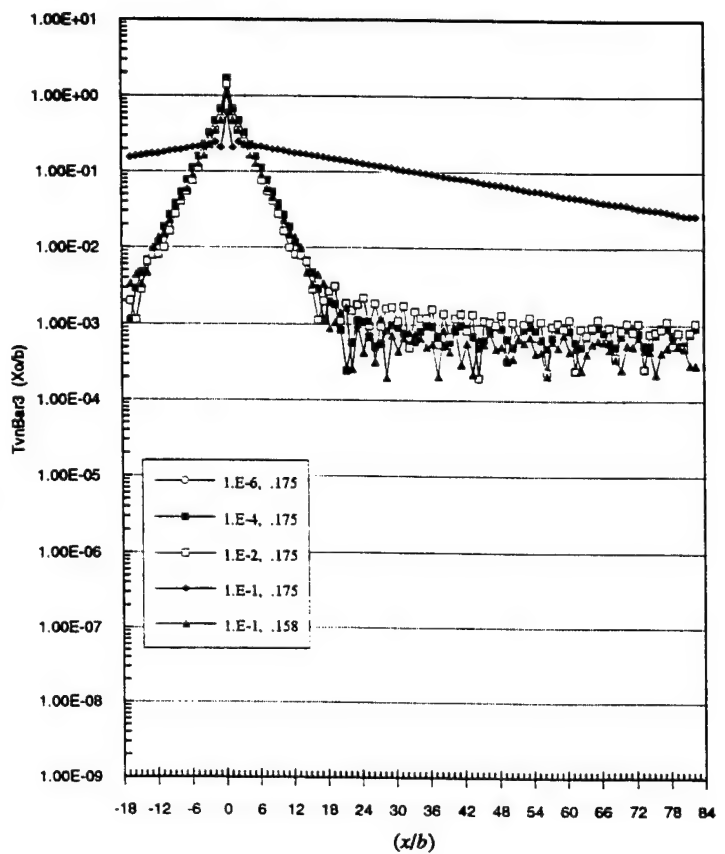


Fig. 14a

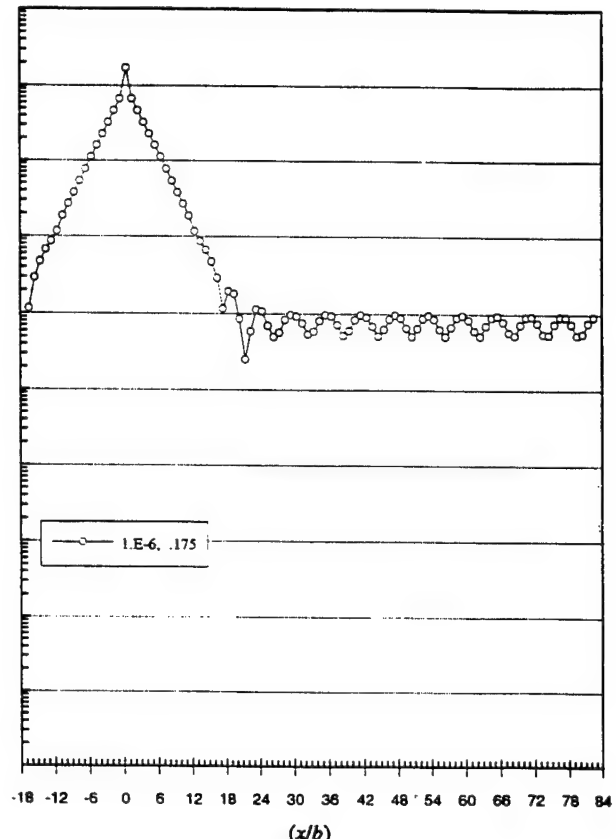


Fig. 14b

Fig. 14. As Fig. 13 but for a natural cylinder.

- a. $(\omega/\omega_c) = 0.175$ with $\varepsilon_c = 10^{-6}, 10^{-4}, 10^{-2}$ and 10^{-1} and $(\omega/\omega_c) = 0.158$ with $\varepsilon_c = 10^{-1}$.
- b. $(\omega/\omega_c) = 0.175$ with $\varepsilon_c = 10^{-6}$.

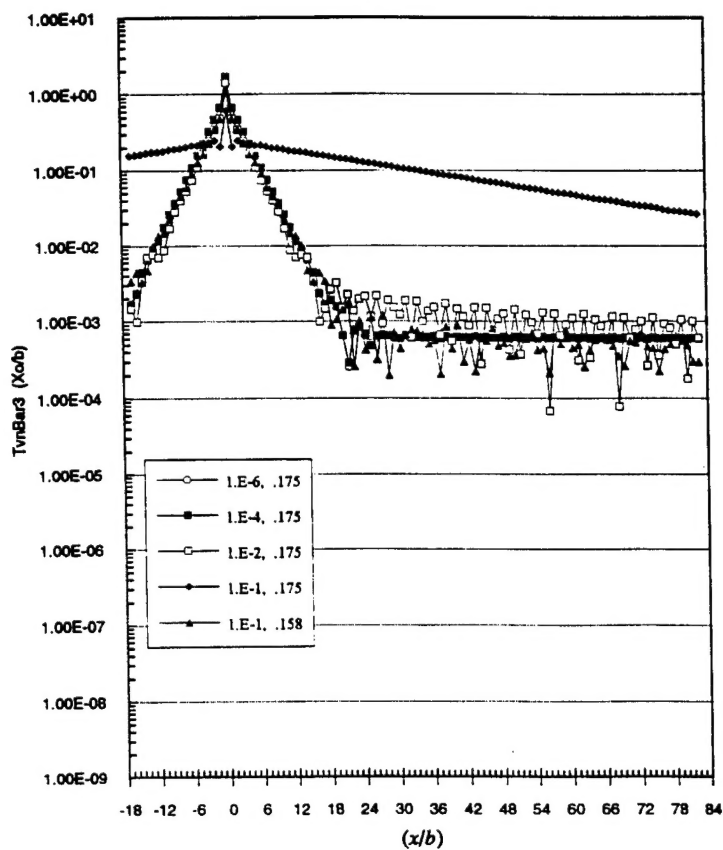


Fig. 15a

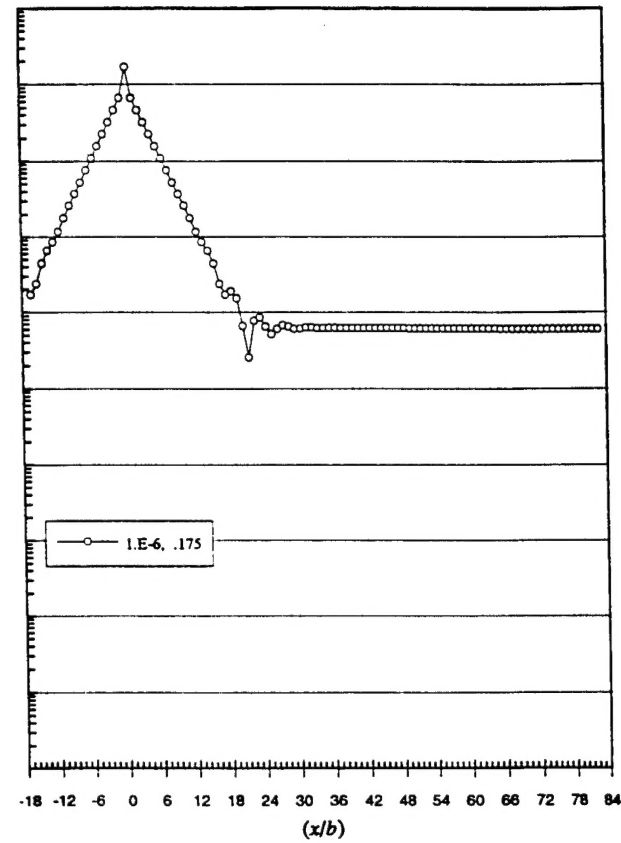


Fig. 15b

Fig. 15. As Fig. 14 except (n) is changed from the standard value of unity to zero.

- a. $(\omega/\omega_c) = 0.175$ with $\epsilon_c = 10^{-6}, 10^{-4}, 10^{-2}$ and 10^{-1} and $(\omega/\omega_c) = 0.158$ with $\epsilon_c = 10^{-1}$.
- b. $(\omega/\omega_c) = 0.175$ with $\epsilon_c = 10^{-6}$.

REFERENCES

1. G. Maidanik and K.J. Becker, "A double-sum technique for performing a Fourier transformation on an integrand composed of aliased factors," NSWCCD-SIG-96/060-7030 (1996).
2. G. Maidanik and K.J. Becker, "Phenomena of aliasing and pass and stop bands in the drive in lieu of ribs on cylindrical shells," NSWCCD report no. SIG-96/072-7030 (1996).
3. L. Cremer, M. Heckl, and E. Ungar, Structure-Borne Sound, Structural Vibrations and Sound Radiation at Audio Frequencies, (Springer-Verlag, 2nd Ed., 1988).
4. M.C. Junger and D. Feit, Sound Structures, and Their Interaction, (MIT Press, 1986).
5. F. Fahy, Sound and Structural Vibration (Radiation, Transmission and Response), (Academic Press, 1985).
6. M.P. Norton, Fundamentals of Noise and Vibration Analysis for Engineers, (Cambridge University Press, 1989).
7. P. Morse and K.U. Ingard, Theoretical Acoustics, (McGraw-Hill Book Company, 1968).
8. C.B. Burroughs, "Acoustic radiation from fluid-loaded infinite circular cylinders with doubly periodic ring supports," J. Acoust. Soc. Am., 75, 715-722 (1984).
9. W. Vogel and D. Feit, "Response of a point excited infinitely long cylindrical shell immersed in an acoustic medium," DTNSRDC report no. 80/061 (1980).
10. Y. Liu and A. Tucker, "The distribution of radiated and vibratory powers of a point-driven infinite cylindrical shell, Part I-Uncoated structure," DTNSRDC report no. 84/043 (1984) and "Part II-Structures with a compliant coating," DTNSRDC report no. 84/044 (1984).
11. G. Maidanik and J. Dickey, "Acoustic behavior of ribbed panels," J. of Sound and Vib., 123, 293-307 (1988).

12. G. Maidanik and J. Dickey, "Velocity distributions on unloaded finitely and regularly ribbed membranes," *J. Acoust. Soc. Am.*, 149, 43-70 (1991) and "Response of regularly ribbed fluid loaded panels," *J. Acoust. Soc. Am.*, 155, 481-495 (1992).
13. G. Maidanik and A.J. Tucker, "Proper and first order solutions of regularly ribbed panels," *J. of Sound and Vib.*, 55, 267-274 (1976).
14. K.J. Becker, "On the response of regularly ribbed cylindrical shell," a thesis in preparation.

INITIAL DISTRIBUTION

Copies

3 NAVSEA 03T2
 2 Taddeo
 1 Becker
 4 ONR/ONT
 1 334 Vogelsong
 1 334 Tucker
 1 334 Main
 1 Library

4 NRL
 1 5130 Bucaro
 1 5130 Williams
 1 5130 Photiadis
 1 Library

4 NUWC/New London
 1 Sandman
 1 Harari
 1 3332 Lee
 1 Library

1 NUWC/NPT
 Library

2 DTIC

1 Johns Hopkins University
 Green

1 Applied Physics Lab
 Johns Hopkins University
 Library

4 ARL/Penn State University
 1 Biancardi
 3 Burroughs

1 Cambridge Collaborative
 Manning

1 Georgia Tech/M.E. Dept.
 Ginsberg

1 MIT
 Dyer

Copies

1 Penn State University
 1 Koopman

2 Virginia Tech
 1 Knight
 1 Fuller

CENTER DISTRIBUTION

Copies Code Name

1	011
1	0112 Douglas
1	0112 Halsall

1	20
1	204
1	2040 Everstine

1	2042
1	2042 Hambric

1	70
---	----

1	7030
---	------

1	7200 Hwang
---	------------

1	7250
1	7250 Maga
1	7250 Vasudevan

1	726 Szilagy
1	804.1 Dickey

2	3421 (TIC-Carderock)
---	----------------------